



Trace element partitioning between garnet lherzolite and carbonatite at 6.6 and 8.6 GPa with applications to the geochemistry of the mantle and of mantle-derived melts

Rajdeep Dasgupta^{a,b,*}, Marc M. Hirschmann^c, William F. McDonough^d,
Marc Spiegelman^b, Anthony C. Withers^c

^a Department of Earth Science, Rice University, 6100 Main Street, MS-126, Houston, TX 77005, USA

^b Lamont-Doherty Earth Observatory, Columbia University, 61 Route 9W, Palisades, NY 10964, USA

^c Department of Geology and Geophysics, University of Minnesota, 310 Pillsbury Drive SE, Minneapolis, MN 55455, USA

^d Department of Geology, University of Maryland, College Park, MD 20742, USA

ARTICLE INFO

Article history:

Accepted 4 February 2009

Keywords:

Carbonatite
Lherzolite
Mantle geochemistry
MORB
OIB
Trace elements

ABSTRACT

We present experimental determinations of trace element partitioning between natural fertile lherzolite and near-solidus carbonatitic liquid (cbl) at pressures of 6.6 and 8.6 GPa and temperatures between 1265 and 1470 °C, conditions relevant for initial generation of CO₂-rich melt beneath oceanic ridges and for carbonate melt percolation in the deep source regions of ocean island basalts. Compared to previous experiments at lower pressures, which produced more aluminous cpx, our experimental cpx–melt pairs show lower partition coefficients for trivalent cations entering the M2 site ($D_{\text{Lu}}^{\text{cpx/cbl}} = 0.17$, $D_{\text{La}}^{\text{cpx/cbl}} = 0.006$). $D_{\text{U}}^{\text{cpx/cbl}}$ (0.002) and $D_{\text{Th}}^{\text{cpx/cbl}}$ (0.001) also are distinctly lower than previous estimates. The garnet–carbonate melt partition coefficients for REE vary from highly incompatible La to moderately compatible Lu and are slightly lower than those from lower pressure experiments. From 6.6 to 8.6 GPa, HFSEs including Zr, Hf, and Ti range from moderately incompatible to slightly compatible, with $D_{\text{Hf}}^{\text{garnet/cbl}} > D_{\text{Ti}}^{\text{garnet/cbl}} > D_{\text{Zr}}^{\text{garnet/cbl}}$. U and Th remain highly incompatible in garnet at both pressures with $D_{\text{U}}^{\text{garnet/cbl}}/D_{\text{Th}}^{\text{garnet/cbl}}$ of 1.2–1.25 at 6.6 GPa and 1.35 at 8.6 GPa. Estimates of $D_{\text{U}}^{\text{gt.lherzolite/cbl}}$, based on our newly measured partition coefficients, suggest that 30–60% of some of the highly incompatible elements can be removed by efficient extraction of 0.1% carbonatitic melt from the Earth's deep upper mantle, and that 0.1% C-rich melt extraction can create a residue that has Rb/Sr, U/Pb and Th/U ratios, respectively, 29, 12, and 6% lower and Sm/Nd ratio ~11% higher than the unmelted source. Our data also suggest that ancient carbonate melt extraction and metasomatism can decouple the Hf and Nd isotope systems. Garnet lherzolite derived carbonatitic melt has lower normalized HREEs and smaller Nb/Ta ratios than erupted natural carbonatites. Therefore, the trace element abundances of erupted carbonatites require either reaction with a shallower mantle peridotite with low modal garnet or derivation from an enriched source. The trace element abundances of deep carbonate-rich melts must become diluted by greater volumes of silicate melt produced in the shallower portions of sub-ridge basalt source regions. But, the observed ²³⁰Th and ²³¹Pa excesses and variations of CO₂/Nb in erupted MORBs are a likely consequence of variable contributions of carbonate-rich melt.

© 2009 Elsevier B.V. All rights reserved.

1. Introduction

Partial melting in the upper mantle plays a crucial role in the ongoing chemical differentiation of the Earth. While the most dominant melting of the mantle occurs chiefly at depths less than 60–70 km under mid oceanic ridges, the onset of melting can occur deeper owing to the agency of trace C–O–H volatiles. The deepest

initiation of partial melting beneath mid-oceanic ridges and oceanic islands is thought to produce incipient carbonatitic melts (Presnall et al., 2002; Dasgupta and Hirschmann, 2006, 2007a). The carbonatitic partial melts generated at great depth from peridotite with 50–200 ppm carbon influence Earth's geochemical evolution by releasing highly incompatible trace elements and volatiles (Galer and O'Nions, 1986; Plank and Langmuir, 1992; Dasgupta et al., 2004; Dasgupta and Hirschmann, 2006). Small-degree carbonatite melts can be strongly enriched in heat producing elements (U, Th, K), rare gases and heavy alkalis, alkali–earths (Cs, Rb, Ba), and LREEs, and removal of such melts can leave residual peridotite correspondingly depleted of these elements. Significant trace element enrichments in natural, erupted

* Corresponding author. Department of Earth Science, Rice University, 6100 Main Street, MS-126, Houston, TX 77005, USA. Tel.: +1 713 348 2664; fax: +1 713 348 5214.
E-mail address: Rajdeep.Dasgupta@rice.edu (R. Dasgupta).

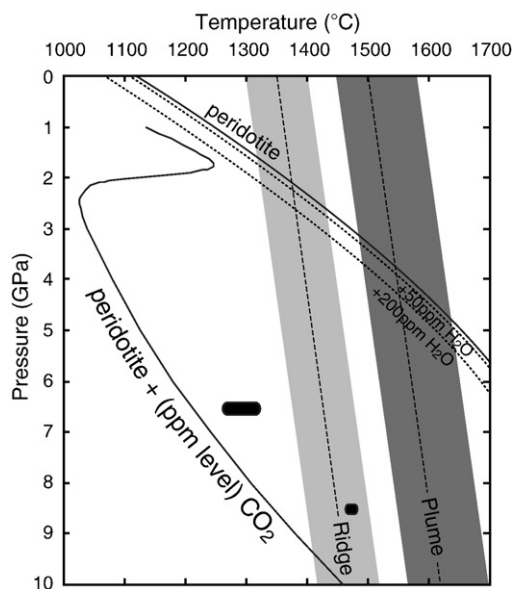


Fig. 1. Pressure–temperature plot showing the location of the solidus for volatile-free, fertile peridotite (Hirschmann, 2000), peridotite with 50–200 ppm H₂O (Aubaud et al., 2004), and peridotite with ~100–1000 ppm CO₂ (Falloon and Green, 1989; Dasgupta and Hirschmann, 2006, 2007a). The solidus of peridotite + CO₂ is constrained by the experiments of Falloon and Green (1989) between 1 and 3 GPa and by the experiments of Dasgupta and Hirschmann (2006, 2007a) between 3 and 10 GPa. The light grey and dark grey shaded bands reflect the mantle adiabats beneath oceanic ridges and hotspots, with the preferred averages indicated by dashed lines. Based on the intersection of the peridotite + CO₂ solidus with the mantle geotherms, initiation of melting is predicted at ~10 GPa for ridges and 12–14 GPa for oceanic islands. Also shown are the conditions for trace element partitioning experiments presented in this study (black capsules).

carbonatites (Nelson et al., 1988; Hoernle et al., 2002) suggest that extreme elemental fractionation is established through carbonatite formation. Also the key radiogenic parent–daughter pairs, for example, U–Th–Pb–He and K–Ar, Rb–Sr, and Sm–Nd, may be fractionated in peridotite depleted by carbonatite removal and in the enriched small-degree carbonatitic melt. Thus, if stored for long, both the carbonatite extracted residue and the carbonatite implanted metasomatized mantle lithology may evolve as geochemical reservoirs with distinct isotopic signatures. However, constraints on the partitioning of the key trace elements between the peridotitic residue and carbonatitic melts are lacking at conditions of initiation of partial melting beneath ridges, i.e., at depths of 200–300 km (Fig. 1: Dalton and Presnall, 1998; Dasgupta and Hirschmann, 2006).

Previous experimental studies have documented trace element partitioning between carbonate melt and the principal mantle minerals including cpx, garnet, opx, amphibole, and olivine, but these are limited to relatively low pressures (≤ 5.5 GPa) compared to those likely to be applicable to initial generation of carbonatite partial melts in the oceanic upper mantle (Fig. 1). Moreover, most of the data are for cpx–melt pairs (Brenan and Watson, 1991; Green et al., 1992; Klemme et al., 1995; Sweeney et al., 1995; Blundy and Dalton, 2000; Adam and Green, 2001) and partition coefficients between garnet and carbonate melts are particularly limited, with no available experimental measurements for most of the REEs, or for a number of elements important to isotopic evolution (Nd, Hf, U, Th, or Pb). Experimentally determined partition coefficients for some of these key elements, including U and Th, are also lacking between natural mantle cpx and carbonate melt. In addition, the cpx compositions for the available cpx/carbonate melt pairs are too aluminous (e.g., 6.61–9.87 wt.%: Adam and Green, 2001; 4.75–7.21 wt.%: Klemme et al., 1995; 6.7–8.6 wt.%: Blundy and Dalton, 2000) to be applicable to carbonate melt generation from lherzolite at a depth of 200–300 km, a condition where residual cpx typically has

1.2–2.5 wt.% Al₂O₃ (Dasgupta, 2006; Dasgupta and Hirschmann, 2007a,b). This limited dataset results in significant uncertainties in the estimated bulk lherzolite–carbonate melt partition coefficients for elements (Dasgupta and Hirschmann, 2006) that are required to evaluate the geochemical consequence of generation of CO₂-rich melts in the deeper portions of the upper mantle.

Here we present new trace element partitioning experiments between peridotitic minerals and near-solidus carbonatitic melt at 6.6 and 8.6 GPa, that are relevant to the initial generation of partial melt in upwelling oceanic mantle (Fig. 1). Based on our newly measured cpx–melt and garnet–melt partition coefficients, we derive better estimates of bulk partition coefficients between lherzolite and carbonatitic melt for a range of trace elements including alkali earth elements, REEs, HFSEs, U, and Th.

2. Experimental methods

2.1. Starting materials

The starting material used for the experiments is based on the composition of carbonatitic melt composition determined near the natural carbonated lherzolite solidus at 6.6 GPa and 1245 °C (Dasgupta and Hirschmann, 2007b). It was prepared from reagent grade CaCO₃, Na₂CO₃, Mg₂SiO₄, FeO, TiO₂, Al₂O₃, and natural magnesite and siderite. To ensure saturation of a peridotitic mineral assemblage and to enhance abundance and growth of garnet and cpx, 10 wt.% each of MixKLB-1 lherzolite powder (Dasgupta and Hirschmann, 2006), a natural cpx, and garnet were added to the carbonate-rich melt (Table 1). Trace elements were added from a mixture of 26 elements (Ba, Ce, Co, Cr, Cs, Dy, Er, Eu, Gd, Hf, La, Lu, Nb, Nd, Ni, Rb, Re, Sc, Sm, Sr, Ta, V, Y, Yb, Zn, Zr) prepared from oxides, carbonates, and nitrates, to which U and Th were added from 1000 ppm AAS standard solutions in 5% HNO₃. Following a denitrification step, ~1.5 wt.% of the trace element mix was added to the carbonate/silicate starting material, thereby introducing 100–1000 ppm of each trace element. These were homogenized in an automated mortar under ethanol and stored at a drying oven at 110–120 °C.

Table 1
Composition of the starting material.

	Melt ^a	Cpx ^b	Gt ^c	MixKLB-1 ^d	Mix ^e
SiO ₂	4.08	52.64	4.132	44.54	16.72
TiO ₂	1.16	0.33	0.07	0.21	0.87
Al ₂ O ₃	0.34	6.00	22.69	3.70	3.48
Cr ₂ O ₃	0.00	0.86	1.75	0.23	0.28
FeO	7.68	2.25	11.76	8.08	7.59
MnO	0.00	0.07	0.39	0.14	0.06
MgO	22.19	15.52	17.08	39.30	22.72
CaO	21.19	20.85	5.05	3.52	17.78
Na ₂ O	4.22	1.47	0.02	0.29	3.13
K ₂ O	0.00	0.01	0.01	0.01	0.00
CO ₂	39.17				27.41
Sum	100.03	100.00	100.13	100.01	100.04
Weight fractions	0.70	0.10	0.10	0.10	

^a Carbonate-rich melt was synthesized by mixing natural magnesite and siderite from University of Minnesota's mineral collection and reagent grade CaCO₃, Na₂CO₃, forsterite, FeO, TiO₂, and Al₂O₃ and is an equilibrium near-solidus melt composition of natural carbonated peridotite as determined at 6.6 GPa (Dasgupta and Hirschmann, 2007b).

^b Natural clinopyroxene from Damaping spinel lherzolite.

^c Natural garnet from Norwegian garnet peridotite.

^d MixKLB-1 is the fertile peridotite composition prepared by mixing natural mineral separates (Dasgupta and Hirschmann, 2006).

^e Major element composition of the starting mix used in this study.

2.2. Experimental strategy

Experiments were performed in either Au or Au₈₀Pd₂₀ capsules with 2 mm outer diameter. The trace element doped starting mix was loaded into the capsules and kept in a drying oven at 120 °C for a couple of hours prior to welding the capsule. After welding, the capsules were pressed in a die to make 2–3 mm long compacted cylinders with 2 mm diameter. High-pressure phase equilibria experiments were performed at 6.6 and 8.6 GPa in a Walker-style multi-anvil apparatus at the University of Minnesota following the cell assembly and calibrations described and reported in Dasgupta et al. (2004).

In trace element partitioning experiments, it is desirable to obtain a small number of large, homogeneous grains of the mineral of interest, coexisting with large pools of melt. Initial experiments were run in Au capsules, directly up to temperature and resulted in carbonatitic melt coexisting with cpx, garnet, opx, and olivine, but the cpx and garnet grains were generally too small (<10 μm) for laser ablation analysis. Only one experiment (M328), run in an Au capsule for 96 h, grew cpx that were large enough for LA-ICP-MS analysis. To facilitate growth of cpx and garnet grains, further experiments were performed in Au–Pd capsules, where temperature at the beginning of each run were raised ~100–250 °C above the final desired run temperature (Table 2, T_i) and held there for 0.5 to 2 h. Temperature overstepping significantly reduced the number of nuclei available for grain growth, although the use of AuPd capsules resulted in significant iron loss in many runs (see the section of Attainment of equilibrium and Fe-loss). After the initial overheating, temperature was lowered at 0.2–0.5 °C/min to the final run temperature, T_f and held there for 24 to 48 h. This strategy yielded modest sized cpx (up to 200 μm) and garnet (up to 30 μm) crystals (Fig. 3) that were analyzable by laser ablation.

3. Analytical techniques

3.1. Electron microprobe analysis

Major-element concentrations in minerals and quenched melt were determined by wavelength-dispersive spectrometry (WDS) using the JEOL 8900JXA electron microprobe at the University of Minnesota with an accelerating voltage of 15 kV, a beam current of 10 nA, and ZAF data reduction. The electron beam was fully focused for the analyses of silicate mineral phases and defocused to 5 μm diameter for magnesite and to 30–50 μm for quenched carbonatite melt. Counting times for all elements were 20 s on the peak and 10 s on each background. Primary standards for minerals and melts were natural cpx (Ca, Mg, Fe, Si), garnet (Ca, Mg, Fe, Al, Si), opx (Mg, Fe, Si), forsterite (Mg, Si), hornblende (Ti), hortonolite (Mn), omphacite (Na), orthoclase (K), dolomite (Ca, Mg), siderite (Fe), and chromite (Cr). A natural basaltic glass was used as a secondary standard. CO₂ for crystalline carbonate was determined by stoichiometry and that for quenched melt by difference of 100% and the analytical total.

Table 2
Summary of the experiments.

Run no.	Capsule	T_i (°C)	T_f (°C)	t at T_i (h)	t at T_f (h)	Ramp from T_i to T_f (degree/min)	Phase assemblage
M319	Au–Pd	1520	1265	0.5	48	0.5	ol + cpx + gt + mst + melt
M312	Au–Pd	1500	1260	0.5	24	0.2	opx + cpx + gt + mst + melt
M318	Au–Pd	1500	1285	0.5	24	0.5	opx + cpx + gt + mst + melt
M341	Au–Pd	1550	1310	2	24	0.5	opx + cpx + gt + mst + melt
M328	Au	–	1320	–	96	–	ol + opx + cpx + gt + mst + melt
M321	Au–Pd	1500	1320	0.5	24	0.5	opx + cpx + gt + mst + melt
M335	Au–Pd	1570	1470	1	24	0.5	opx + cpx + gt + mst + melt

All the experiments except M335 are conducted at 6.6 GPa. M335 is conducted at 8.6 GPa. ol, olivine; cpx, clinopyroxene; gt, garnet; mst, magnesite; melt, carbonatitic melt. T_i and T_f are initial and final temperature respectively.

3.2. Laser ablation-ICP-MS analysis

Trace element concentrations of the quenched carbonatitic melt and minerals were determined by laser ablation ICP-MS (LA-ICP-MS) at the University of Maryland using a Thermo Scientific Element2 high resolution, single-collector, inductively coupled plasma mass spectrometer (ICP-MS) coupled to a New Wave UP213 frequency-quintupled Nd-YAG laser, which emits 213 nm light. The ablation signal for NIST 610 was maximized on ⁴³Ca and ²³²Th and minimized for oxide production (²³²Th¹⁶O/²³²Th < 0.2%). The standard reference material for the laser ablation analyses was NIST 610. The laser was turned on in a shuttered pre-ablation mode for 20 s prior to each analysis. The NIST 610 and the experimental quenched melt were ablated using line analyses (30 μm diameter spot flashed at 5 Hz and ~1 J/cm², with the spot moving laterally at 10 μm/s) whilst the minerals were analyzed using spot ablations (8–40 μm diameter spots flashed at 4–8 Hz ~1 J/cm², depending on crystal size). Following each analysis, a 2-minute washout period allowed for cleaning and minimized memory effects.

All ablations occurred in a helium (He) atmosphere (~1 L/min flow rate) that was coupled to Ar gas (~0.4 L/min flow rate) downstream at a T-junction prior to its introduction into the plasma torch. Background counts were measured for 20–30 s prior to each ablation followed by ~50 s ablation signal, or shorter times in cases of small (i.e., <30 μm) crystals. Measurements were performed with the ICP-MS using the electrical scan mode (E-scan) and counting mode of detection. Four to seven line scans were conducted in each of the quenched melts. Data were collected for the following masses: ⁴³Ca, ⁴⁵Sc, ⁴⁹Ti, ⁵³Cr, ⁵⁵Mn, ⁵⁹Co, ⁶²Ni, ⁸⁵Rb, ⁸⁶Sr, ⁸⁹Y, ⁹⁰Zr, ⁹³Nb, ¹³³Cs, ¹³⁷Ba, ¹³⁹La, ¹⁴⁰Ce, ¹⁴⁶Nd, ¹⁴⁷Sm, ¹⁵³Eu, ¹⁵⁷Gd, ¹⁶³Dy, ¹⁶⁷Er, ¹⁷²Yb, ¹⁷⁵Lu, ¹⁷⁸Hf, ¹⁸¹Ta, ¹⁸⁵Re, ²⁰⁸Pb, ²³²Th, and ²³⁸U. Analyses of unknowns were accompanied by the analysis of SRM NIST 610 before and after the sample acquisition, which provided the calibration curves for determining element concentrations and for constraining instrument drift. Data were processed using the LAMTRACE (Achterbergh et al., 2001) software program, which determines element concentrations based on ratios of count rates for samples and standards, known concentrations in the standards, and the known concentration of an internal standard element in the unknowns. Detection limits for each spot or line analysis can differ considerably from element to element depending on background, count rate, and laser ablation parameters. In all case data are reported for signals that are distinguishable at 3 s.d. above background.

4. Results

4.1. Phase assemblage and texture

Each of the experiments produced an assemblage of cpx + garnet + magnesite + quenched carbonatitic melt ± olivine ± opx (Table 2). Modes obtained by mass balance calculation show that at 6.6 GPa, 54–56 wt.% carbonatitic melt coexists with ~18 wt.% garnet, 0–2 wt.% cpx, 8–11 wt.%

magnesite, with the remainder consisting of olivine and/or opx. At 8.6 GPa, ~65 wt.% carbonatitic melt coexisted with ~11 wt.% garnet, ~12 wt.% cpx, ~12 wt.% magnesite, and a trace amount of opx.

Typical run products have pools of quenched carbonate melt comprising blades of dolomitic crystals and interstitial oxides and silicates (Fig. 2a–f) present throughout the charge and crystalline silicates and carbonate present at the cooler ends of the cylindrical capsules (e.g., Fig. 2b). Despite conducting crystallization experiments to enhance grain growth, garnet grains in most runs were in the range of 3–10 μm and many of them preserved small, unreacted cores (Fig. 2), indicating

that the initial temperature (T_i) was below the liquidus of the bulk composition. Only three runs (M318, M321, and M335) produced garnet grains large enough for reliable LA-ICP-MS analyses. Cpx grains, however, achieved sizes >100 μm in most runs and no heterogeneity was apparent based on backscattered electron contrast (Fig. 2a, c, d, e).

4.2. Major element compositions

The major element compositions of cpx, garnet, magnesite, and melt are given in “Tables 3–6. The relevance of mineral–melt trace element

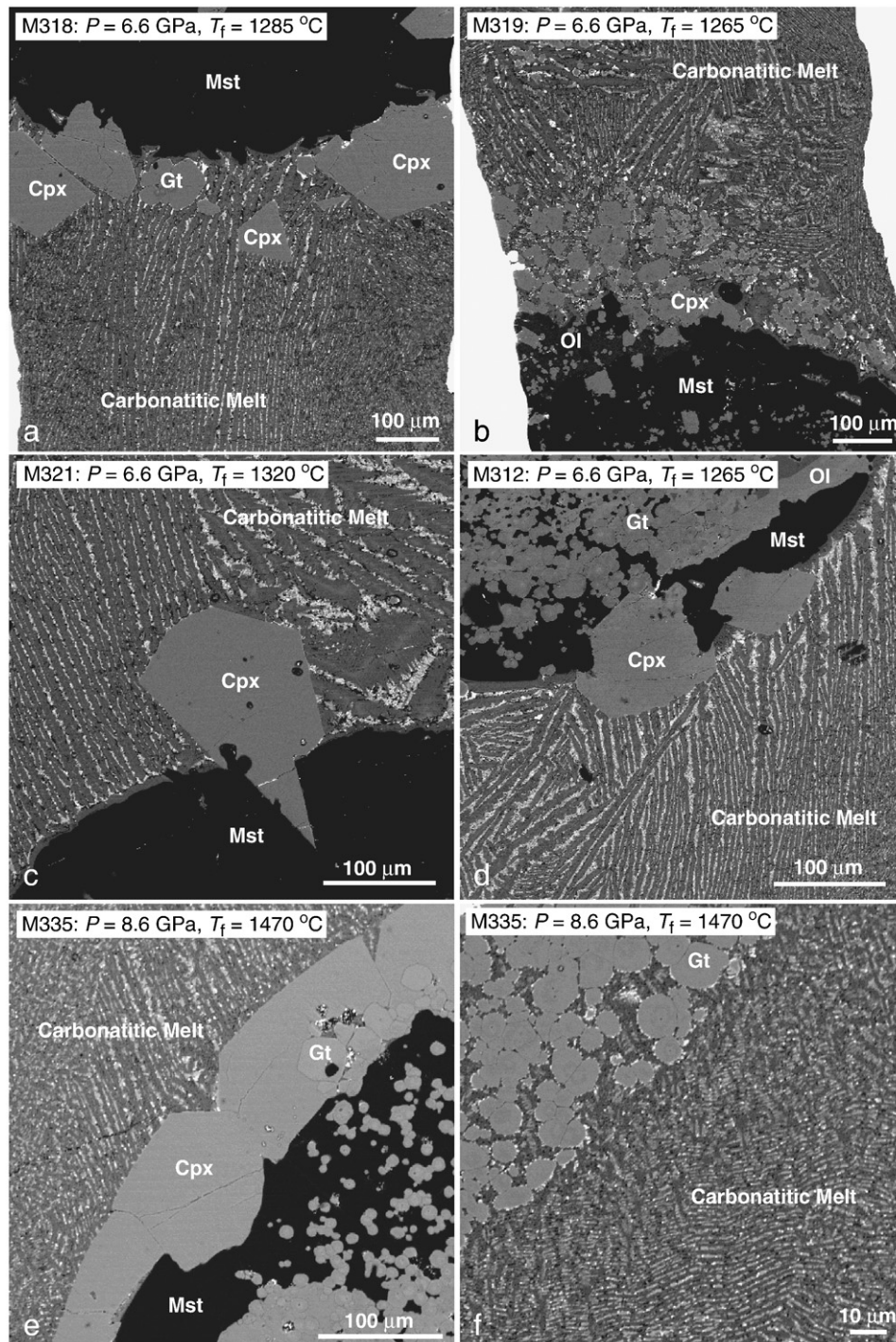


Fig. 2. Back-scattered electron images showing micro-textures from the trace element partitioning experiments conducted in this study. T_f gives the final equilibration temperature for the runs. Cpx—clinopyroxene, Gt—garnet, Mst—magnesite, and Ol—olivine.

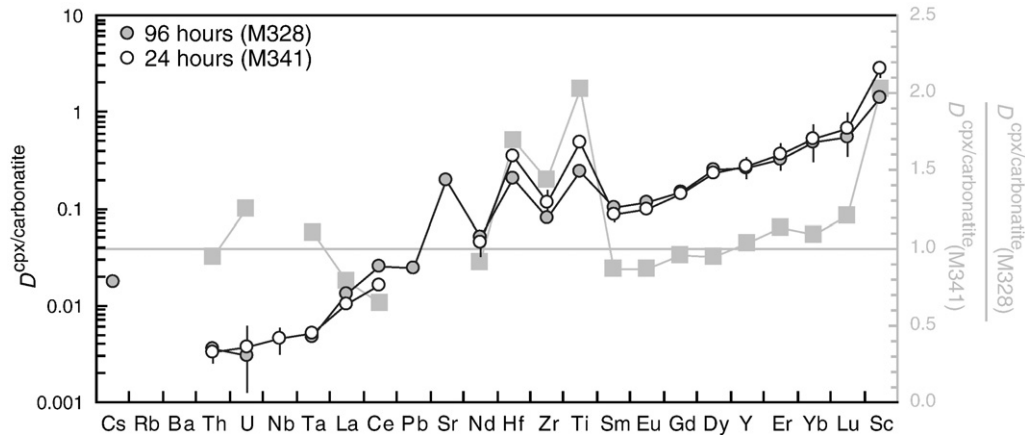


Fig. 3. Clinopyroxene/carbonatitic melt partition coefficients derived from experiments lasting 24 (M341: 6.6 GPa, 1310 °C) and 96 (M328: 6.6 GPa, 1320 °C) hours. The left axis (in black) plots the actual partition coefficients and the right axis (in grey) plots the ratio of partition coefficients from the two experiments. The partition coefficients are nearly identical for nearly all elements with the difference between two experiments not exceeding by a factor of two, indicating that the equilibration of trace elements between coexisting minerals and melts is approached in less than 24 h under the experimental conditions.

partitioning data depends on the major element compositions of the phases of interest. Here we evaluate whether the cpx, garnet, magnesite, and melt compositions from the present study match closely with those expected near the natural carbonated lherzolite solidus at the depth range of 200 to 300 km.

Cpx have 2–5 wt.% Al_2O_3 at 6.6 GPa and 2.3 wt.% at 8.6 GPa (Table 3), which compares favorably to the 2.5 wt.% observed near the solidus of carbonated peridotite at 6.6 GPa (Dasgupta, 2006; Dasgupta and Hirschmann, 2007a,b). The Mg# of the cpx from experiments with minimal Fe-loss (M328, M341, and M335) are in the range 91–92, which

makes them ~1 wt.% less FeO^* -rich than the cpx from comparable phase equilibria experiments. TiO_2 (0.15–0.36 wt.%) and Na_2O (1–2.4 wt.%) contents of the present experiments are also similar to those observed in the previous phase equilibria experiments (0.12–0.26 wt.% TiO_2 and 0.75–1.43 wt.% Na_2O , respectively: Dasgupta, 2006; Dasgupta and Hirschmann, 2007a,b).

Garnet from the experiments that were large enough to analyze for trace elements (M318, M321, M335) are Mg-rich with pyrope content ($100 \times$ molar $\text{Mg}/(\text{Mg} + \text{Mn} + \text{Fe} + \text{Ca})$) of 84–86 at 6.6 GPa and ~77 at 8.6 GPa (Table 4), with grossular ($100 \times$ molar $\text{Ca}/(\text{Mg} + \text{Mn} + \text{Fe} + \text{Ca})$)

Table 3
Major element composition of clinopyroxenes.

Run no.	M319	M312	M318	M341	M328	M321	M335
P (GPa)	6.6	6.6	6.6	6.6	6.6	6.6	8.6
T (°C)	1265	1265	1285	1310	1320	1320	1470
n	9	11	10	8	7	8	12
SiO_2	55.50 (64)	56.25 (32)	55.98 (43)	55.47 (31)	55.37 (26)	56.25 (46)	56.16 (22)
TiO_2	0.36 (3)	0.21 (5)	0.35 (10)	0.36 (8)	0.33 (3)	0.32 (8)	0.15 (3)
Al_2O_3	3.44 (54)	3.33 (28)	4.89 (87)	1.95 (12)	1.75 (11)	4.20 (51)	2.36 (12)
Cr_2O_3	0.45 (15)	0.34 (7)	0.65 (15)	0.36 (10)	0.26 (5)	0.58 (11)	0.36 (5)
FeO^*	1.36 (28)	1.70 (21)	0.50 (38)	2.74 (25)	2.72 (12)	1.12 (37)	3.41 (23)
MnO	0.05 (3)	0.07 (3)	0.07 (3)	0.03 (1)	0.02 (2)	0.07 (4)	0.07 (3)
MgO	17.62 (75)	18.7 (13)	18.1 (29)	17.97 (25)	17.87 (14)	19.4 (20)	20.79 (30)
NiO	0.01 (2)	0.01 (2)	0.01 (2)	0.01 (1)	0.01 (2)	0.02 (2)	0.02 (3)
CaO	19.19 (67)	17.4 (12)	16.6 (23)	20.00 (23)	20.30 (25)	15.7 (19)	15.06 (42)
Na_2O	1.83 (26)	1.75 (20)	2.36 (43)	0.99 (3)	0.95 (5)	2.08 (27)	1.35 (9)
K_2O	0.02 (2)	0.03 (1)	0.02 (1)	0.02 (1)	0.02 (1)	0.02 (1)	0.03 (1)
Sum	99.85	99.75	99.55	99.92	99.62	99.75	99.76
Mg#	95.84	95.16	98.48	92.11	92.12	96.87	91.58
Si	1.982	1.999	1.982	1.994	1.998	1.987	1.999
Al^{IV}	0.018	0.001	0.018	0.006	0.002	0.013	0.001
Al^{VI}	0.127	0.139	0.186	0.077	0.072	0.162	0.099
Fe^{3+}	0.000	0.000	0.000	0.000	0.000	0.000	0.000
Cr	0.013	0.010	0.018	0.010	0.008	0.016	0.010
Ti	0.010	0.006	0.009	0.010	0.009	0.009	0.004
Fe^{2+}	0.041	0.051	0.015	0.083	0.082	0.033	0.102
Ni	0.041	0.050	0.015	0.082	0.082	0.033	0.101
Mn	0.002	0.002	0.002	0.001	0.001	0.002	0.002
Mg	0.938	0.992	0.957	0.963	0.961	1.021	1.104
Ca	0.734	0.661	0.629	0.770	0.785	0.594	0.574
Na	0.127	0.121	0.162	0.069	0.067	0.142	0.093
K	0.001	0.001	0.001	0.001	0.001	0.001	0.001
Sum	4.033	4.032	3.994	4.067	4.068	4.013	4.091

Total Fe is given as FeO^* . Mg# = molar $\text{Mg}/(\text{Mg} + \text{Fe})$. The numbers in the parentheses are 1σ error of the mean and reported as the least unit cited. For example, 55.50 (64) should be read as 55.50 ± 0.64 wt.%. n is the number of analyses averaged.

Table 4
Major element composition of garnets.

Run no.	M312	M318	M341	M321	M335
P (GPa)	6.6	6.6	6.6	6.6	8.6
T (°C)	1265	1285	1310	1320	1470
n	8	7	9	6	12
SiO ₂	43.30 (32)	43.54 (24)	43.24 (40)	43.33 (31)	43.23 (39)
TiO ₂	0.40 (5)	0.50 (5)	0.66 (27)	0.65 (5)	0.66 (7)
Al ₂ O ₃	22.58 (20)	23.17 (31)	22.86 (14)	22.75 (14)	21.67 (30)
Cr ₂ O ₃	1.80 (6)	1.56 (20)	1.67 (6)	1.66 (6)	1.50 (9)
FeO*	3.66 (6)	1.95 (31)	3.09 (16)	3.07 (22)	6.21 (23)
MnO	0.10 (4)	0.16 (2)	0.13 (1)	0.13 (3)	0.11 (3)
MgO	23.89 (25)	24.61 (55)	24.32 (41)	24.50 (15)	22.25 (41)
NiO	0.04 (4)	0.02 (2)	0.01 (1)	0.01 (1)	0.01 (1)
CaO	3.75 (12)	4.00 (64)	3.91 (28)	3.89 (10)	4.37 (28)
Na ₂ O	0.38 (32)	0.30 (19)	0.13 (10)	0.12 (6)	0.09 (2)
K ₂ O	0.02 (1)	0.04 (1)	0.02 (1)	0.02 (1)	0.02 (1)
Sum	99.93	99.83	100.03	100.14	100.13
Si	6.039	6.027	5.999	6.004	6.078
Ti	0.042	0.052	0.069	0.068	0.070
Al	3.712	3.780	3.738	3.715	3.591
Cr	0.199	0.170	0.183	0.182	0.167
Fe	0.427	0.226	0.358	0.356	0.730
Mn	0.012	0.018	0.016	0.015	0.013
Mg	4.967	5.078	5.029	5.061	4.664
Ni	0.005	0.002	0.001	0.001	0.001
Ca	0.560	0.593	0.582	0.578	0.659
Na	0.103	0.080	0.034	0.033	0.025
K	0.004	0.007	0.003	0.003	0.003
Sum	16.070	16.027	16.010	16.013	15.998
Endmembers					
Py	83.25	85.85	84.04	84.21	76.88
Alm	7.16	3.82	5.98	5.92	12.03
Gro	9.39	10.02	9.72	9.62	10.86
Sp	0.19	0.31	0.26	0.26	0.22

Total Fe is given as FeO*. Endmembers: Py (pyrope) = $100 \times \text{Mg}/(\text{Mg} + \text{Fe} + \text{Ca} + \text{Mn})$; Alm (almandine) = $100 \times \text{Fe}/(\text{Mg} + \text{Fe} + \text{Ca} + \text{Mn})$; Gro (grossular) = $100 \times \text{Ca}/(\text{Mg} + \text{Fe} + \text{Ca} + \text{Mn})$; Sp (spessartine) = $100 \times \text{Mn}/(\text{Mg} + \text{Fe} + \text{Ca} + \text{Mn})$. The numbers in the parentheses are 1 σ error of the mean and reported as the least unit cited. For example, 43.30 (32) should be read as 43.30 ± 0.32 wt.%. *n* is the number of analyses averaged.

contents of 9.4–10.0 at 6.6 GPa and 10.9 at 8.6 GPa. The measured grossular contents overlap those observed in the previously determined experimental solidus (grossular content of 9–13; Dasgupta, 2006; Dasgupta and Hirschmann, 2007a,b), although the pyrope contents in the present experiments are somewhat higher than those noted in the previous experiments (pyrope content of 68–72; Dasgupta, 2006; Dasgupta and Hirschmann, 2007a,b). Concentrations of TiO₂ and Cr₂O₃ are 0.40–0.66 wt.% and 1.5–1.8 wt.%, respectively, which is in reasonable agreement with the data previously obtained in natural carbonated lherzolite (0.49–0.96 wt.% TiO₂ and 0.88–1.34 wt.% Cr₂O₃; Dasgupta, 2006; Dasgupta and Hirschmann, 2007a,b) and nominally CO₂-free natural lherzolite (0.1–0.6 wt.% TiO₂ and 2.1–2.2 wt.% Cr₂O₃; Brey et al., 1990, 2008) systems at 6–9 GPa and 1225–1400 °C.

The melts are carbonatitic (cBl) with 41–45 wt.% CO₂ and are calcio-dolomitic to dolomitic in nature (Table 6). Ca# (molar Ca/(Ca + Mg + Fe)) of quenched melt, from runs with minimal Fe-loss, is 0.52–0.58 at 6.6 GPa and 0.42 at 8.6 GPa, and is somewhat higher than that determined for near-solidus carbonate partial melt of lherzolite at 6.6 GPa (~0.37). Respective SiO₂, TiO₂, and Al₂O₃ contents are ~3.1–3.9 wt.%, 1.3–1.7 wt.%, and 0.2–0.3 wt.% at 6.6 GPa and 7.6 wt.%, 1 wt.%, and 0.5 wt.% at 8.6 GPa. Concentration of Na₂O is 3.9–4.0 wt.% at 6.6 GPa and 2.2 wt.% at 8.6 GPa. The carbonatitic melt major element compositional systematics obtained in this study, such as decreases in Ca# and Na₂O and increases in SiO₂ with pressure, are in good agreement with previous near-solidus partial melting studies of peridotite at 6–8 GPa (Dalton and Presnall, 1998; Gudfinsson and Presnall, 2005; Dasgupta and Hirschmann, 2007a,b).

4.3. Attainment of equilibrium

The approach to equilibrium can be tested with the following observations: two of our experiments (M341: 6.6 GPa, 1310 °C and M328: 6.6 GPa, 1320 °C) were conducted in effectively similar conditions but differed in the run duration (M341: 24 h and M328: 96 h) and temperature cycle (M341: *T*_i of 1550 °C for 2 h and 0.5 °C/min cooling down to *T*_f of 1310 °C; M328: static run). The major element compositions of the resulting phases are effectively similar with carbonatitic melt of Mg# ~83.5–83.7 and Ca# ~0.52–0.53 and cpx has Mg# of 92.1. Moreover, the cpx/melt trace element partition coefficients for these two runs, plotted in Fig. 3, are virtually indistinguishable, suggesting that 24 h at ~1310–1320 °C yield reasonably well equilibrated clinopyroxenes in terms of their trace element concentrations. Unfortunately, the trace element concentrations of the garnet and magnesite from these two runs could not be analyzed, owing to the small grain sizes of the former and to abundant garnet inclusions in the latter. However, the major element garnet/melt partition coefficients, including those of Ti (~0.3–0.7), and Ca (0.13–0.20) from our experiments matched the previously determined garnet/melt phase equilibria under similar conditions and using sandwich experiments (Dasgupta and Hirschmann, 2007b).

4.4. Mineral/melt partition coefficients

Trace element concentrations of cpx, garnet, magnesite, and melt are reported in Tables 7 and 8 and resulting mineral/melt partition coefficients are reported in Table 9. Uncertainties in the coefficients are estimated by error propagation from analytical uncertainties in the individual phases given in Tables 7 and 8.

4.4.1. Cpx/carbonate melt trace element partitioning

Trace element partition coefficients for cpx/melt pairs are plotted in Fig. 4, showing the essential features of our new data and comparing them with previously published experimental determinations. Our data are condensed to two trends from different pressures (6.6 and 8.6 GPa), where the data from only the experiments with least Fe-loss have been plotted. The experiments with greater Fe-loss show somewhat lower values of partition coefficients (Fig. 4). The $D^{\text{cpx/cbl}}$ values for REEs, HFSEs, U, and Th from the 8.6 GPa experiment are somewhat lower than those obtained from 6.6 GPa (Fig. 4). The partition coefficients obtained in our experiments are also noticeably smaller than the previous measurements at lower pressures (1.5–5.5 GPa). This is particularly true for elements substituting into the cpx M2 site, including the trivalent cations ($D_{\text{Lu}}^{\text{cpx/cbl}} = 0.17$, $D_{\text{La}}^{\text{cpx/cbl}} = 0.006$). At 8.6 GPa, $D_{\text{U}}^{\text{cpx/cbl}}$ (0.001) and $D_{\text{Th}}^{\text{cpx/cbl}}$ (0.002) are also noticeably lower than the previous estimates.

Our data, combined with previous lower pressure determinations, suggest that $D_{\text{REE}}^{\text{cpx/cbl}}$ decreases with increasing pressure. This could reflect in part pressure dependence to $D_{\text{REE}}^{\text{cpx/cbl}}$. Additionally, it may owe in part to decreasing Al₂O₃ with increasing pressure, as $D_{\text{REE}}^{\text{cpx/cbl}}$ increases with increasing Al₂O₃ in pyroxene (Wood and Blundy, 2001).

4.4.2. Garnet/carbonate melt trace element partitioning

Trace element partition coefficients between garnet and carbonatitic melt are plotted in Fig. 5, showing those determined in our study and comparing them with values determined in previous experiments. The REEs show steady increase in *D*s from highly incompatible La ($D_{\text{La}}^{\text{garnet/cbl}} \sim 0.006 \pm 0.001$ at 6.6 GPa and 0.039 ± 0.004 at 8.6 GPa) to moderately compatible Lu ($D_{\text{Lu}}^{\text{garnet/cbl}} \sim 2.23 \pm 0.27$ at 6.6 GPa and 4.6 ± 0.9 at 8.6 GPa). HFSEs including Zr, Hf, and Ti are moderately incompatible at 6.6 GPa whereas they become slightly compatible at 8.6 GPa. However, at both pressures, $D_{\text{Hf}}^{\text{garnet/cbl}} > D_{\text{Ti}}^{\text{garnet/cbl}} > D_{\text{Zr}}^{\text{garnet/cbl}}$ with $D_{\text{Zr}}^{\text{garnet/cbl}}/D_{\text{Hf}}^{\text{garnet/cbl}}$ of 0.62–0.82 at 6.6 GPa and 0.75 at 8.6 GPa. U

Table 5
Major element compositions of magnesite.

Run no.	M319	M312	M318	M341	M328	M321	M335
P (GPa)	6.6	6.6	6.6	6.6	6.6	6.6	8.6
T (°C)	1265	1265	1285	1310	1320	1320	1470
n	13	11	12	11	10	14	10
SiO ₂	0.01 (2)	0.01 (1)	0.00 (1)	0.00	0.00	0.00	0.00
TiO ₂	0.00	0.01 (1)	0.02 (1)	0.01 (1)	0.01 (1)	0.01 (1)	0.01 (2)
Al ₂ O ₃	0.02 (2)	0.01 (1)	0.03 (1)	0.01 (1)	0.01 (1)	0.04 (2)	0.01 (1)
Cr ₂ O ₃	0.01 (2)	0.01 (1)	0.01 (1)	0.02 (2)	0.02 (2)	0.02 (1)	0.03 (1)
FeO*	2.51 (48)	2.62 (10)	1.09 (16)	5.00 (7)	5.00 (7)	1.53 (27)	4.58 (20)
MnO	0.11 (2)	0.09 (2)	0.10 (1)	0.09 (2)	0.09 (2)	0.12 (3)	0.09 (2)
MgO	38.96 (61)	41.29 (34)	40.36 (64)	39.10 (29)	39.10 (29)	40.79 (53)	41.29 (23)
NiO	0.03 (2)	0.01 (2)	0.02 (2)	0.01 (1)	0.01 (1)	0.02 (2)	0.03 (3)
CaO	8.0 (10)	5.18 (23)	7.66 (88)	5.60 (25)	5.60 (25)	6.71 (64)	3.39 (16)
Na ₂ O	0.03 (2)	0.17 (4)	0.03 (3)	0.08 (6)	0.08 (6)	0.04 (2)	0.04 (4)
K ₂ O	0.01 (1)	0.02 (1)	0.03 (1)	0.01 (1)	0.01 (1)	0.02 (1)	0.02 (1)
CO ₂	50.44 (98)	50.81 (31)	50.79 (17)	50.21 (9)	50.21 (9)	50.85 (30)	50.65 (39)
Sum	100.10	100.23	100.13	100.13	100.13	100.13	100.15
Mg#	96.52	96.56	98.50	93.31	93.31	97.94	94.14
Ca#	0.12	0.08	0.12	0.09	0.09	0.10	0.05

Total Fe is given as FeO*. Mg# = 100 × molar Mg/(Mg + Fe). Ca# = molar Ca/(Ca + Mg + Fe). The numbers in the parentheses are 1σ error of the mean and reported as the least unit cited. For example, 0.01 (1) should be read as 0.01 ± 0.01 wt.%. n is the number of analyses averaged.

and Th remain highly incompatible in garnet at both pressures, with $D_{\text{U}}^{\text{garnet/cbl}}/D_{\text{Th}}^{\text{garnet/cbl}}$ of 1.2–1.25 at 6.6 GPa and 1.35 at 8.6 GPa. The new determinations of $D_{\text{U}}^{\text{garnet/cbl}}$ are broadly similar to previously determined trace element partition coefficients between garnet and carbonatitic melt at 2.5–4.6 GPa (Fig. 5), with the chief difference being smaller partition coefficients for the middle to heavy rare earth elements in the higher pressure experiments.

5. Discussion

5.1. Crystal chemistry control on trace element partitioning—lattice strain energy modeling

The lattice strain theory developed by Brice (1975) among others and employed by Blundy and Wood (1994, 2003) is a useful framework for evaluating the influence of crystal chemistry on mineral/melt partition coefficients. The mineral/melt partition coefficients (D_i) of

isovalent cations in a particular lattice site are parameterized in terms of a near-parabolic dependence on ionic radius—

$$D_i = D_0 \exp \left[\frac{-4\pi N_A \left[\frac{r_i}{2} (r_i - r_0)^2 + \frac{1}{3} (r_i - r_0)^3 \right]}{RT} \right] \quad (1)$$

where E is an effective Young's modulus for the site, r_i is the radius of the substituting cation and r_0 is the radius of a hypothetical cation that substitutes into the site with zero strain, D_0 is the partition coefficient for that hypothetical cation, N_A is Avogadro's number, R is the gas constant, and T is temperature in Kelvins. In this section we apply this lattice strain model to examine the systematics of our partitioning data between cpx and carbonatitic melt and garnet and carbonatitic melt.

5.1.1. Lattice strain model for cpx–carbonate melt partitioning

For substitution of 2+ and 3+ cations into the M2 site of cpx, the parameters r_0 , E_{M2} , and D_0 were fitted to the experimental data by a

Table 6
Major element compositions of melt.

Run no.	M319	M312	M318	M341	M328	M321	M335
P (GPa)	6.6	6.6	6.6	6.6	6.6	6.6	8.6
T (°C)	1265	1265	1285	1310	1320	1320	1470
n	11	12	9	11	14	12	15
SiO ₂	2.97 (40)	5.11 (30)	3.88 (44)	3.10 (26)	3.88 (20)	4.35 (80)	7.64 (71)
TiO ₂	1.58 (16)	1.79 (12)	1.69 (20)	1.71 (21)	1.28 (8)	1.86 (29)	1.02 (10)
Al ₂ O ₃	0.34 (6)	0.67 (4)	0.61 (6)	0.31 (6)	0.17 (3)	0.56 (10)	0.48 (5)
Cr ₂ O ₃	0.04 (3)	0.05 (4)	0.04 (3)	0.04 (2)	0.02 (1)	0.03 (3)	0.04 (3)
FeO*	1.34 (9)	2.44 (13)	0.43 (8)	5.25 (21)	5.30 (24)	0.84 (14)	4.97 (19)
MnO	0.08 (5)	0.12 (3)	0.07 (4)	0.11 (3)	0.10 (4)	0.10 (3)	0.09 (2)
MgO	13.42 (27)	15.01 (28)	13.94 (21)	15.11 (18)	15.01 (28)	14.99 (39)	18.92 (18)
NiO	0.02 (3)	0.02 (3)	0.02 (3)	0.03 (3)	0.03 (5)	0.03 (3)	0.02 (3)
CaO	31.89 (38)	29.43 (41)	30.17 (49)	27.55 (67)	28.67 (37)	29.85 (84)	21.86 (22)
Na ₂ O	3.47 (32)	2.51 (32)	4.50 (96)	4.01 (39)	3.91 (14)	3.37 (49)	2.24 (23)
K ₂ O	0.05 (2)	0.03 (2)	0.05 (2)	0.03 (1)	0.02 (1)	0.05 (1)	0.03 (2)
CO ₂	44.81 (39)	42.82 (41)	44.59 (38)	42.75 (45)	41.61 (74)	43.98 (61)	42.68 (84)
Sum	100.00	100.00	100.00	100.00	100.00	100.00	100.00
Mg#	94.69	91.66	98.31	83.69	83.48	96.95	87.15
Ca#	0.62	0.56	0.60	0.52	0.53	0.58	0.42

Total Fe is given as FeO*. Mg# = 100 × molar Mg/(Mg + Fe). Ca# = molar Ca/(Ca + Mg + Fe). The numbers in the parentheses are 1σ error of the mean and reported as the least unit cited. For example, 2.97 (40) should be read as 2.97 ± 0.40 wt.%. n is the number of analyses averaged.

Table 7
Trace element compositions of clinopyroxenes and melts.

Run no.	M319		M312		M318		M341		M328		M321		M335		M319		M312		M318		M341		M328		M321		M335	
P(GPa)	6.6		6.6		6.6		6.6		6.6		6.6		8.6		6.6		6.6		6.6		6.6		6.6		6.6		8.6	
T (°C)	1265		1265		1285		1310		1320		1320		1470		1265		1265		1285		1310		1320		1320		1470	
Phase	Melt		Melt		Melt		Melt		Melt		Melt		Melt		Cpx		Cpx		Cpx		Cpx		Cpx		Cpx		Cpx	
n	7/7		4/4		5/5		4/4		4/4		4/4		4/4		2/1		6/5		5/3		2/2		4/1		3/3		5/5	
	Mean	1σ	Mean	1σ	Mean	1σ	Mean	1σ	Mean	1σ	Mean	1σ	Mean	1σ	Mean	Mean	1σ	Mean	1σ	Mean	1σ	Mean	1σ	Mean	Mean	1σ	Mean	1σ
Sc	96	9	143	7	143	19	55	9	61	3	142	21	96	7	132	121	5	160	7	155	19	84	138	4	67	71	11	
Ti	8468	1400	9186	553	10,620	2016	5354	611	7156	363	11,105	1873	5038	361	1485	1091	120	2239	246	2642	281	1753	1803	44	721	71	269	
Cr	194	36	207	22	329	62	64	11	100	2	302	43	243	34	2506	2972	531	4585	559	2188	659	1426	2964	290	2347	81	18	
Mn	753	79	791	61	781	93	634	49	728	14	855	125	708	126	366	562	101	321	7	410	127	306	369	8	469	81	18	
Co	41.3	5.1	59	3	13.3	1.6	57	3	58	2	24	2	85	9	49	57	10	10.2	1.9	54	13	40	21	2	81	18	18	
Ni	<276		<161		<216		<258		<198		<138		<336		<1902	<886		<576		<858		<451	<159		<600			
Rb	613	117	220	51	1094	368	414	41	584	22	746	111	197	30	<103	<36		14.0	5.2	<34		<31	<8		<60			
Sr	631	64	433	21	585	105	588	37	501	40	516	64	309	49	<179	<121		15.8		<90		97	17		<156			
Y	352	41	342	24	400	79	211	26	194	7	367	50	209	18	45	32	2	30	3	57	15	51	31	1	27	6	0	
Zr	403	59	346	11	458	95	233	27	242	10	448	75	188	14	18	12	1	27	5	27	11	20	21	1	5	0	0	
Nb	409	61	329	20	436	88	329	40	414	15	439	84	197	22	<3	0.4	0.2	0.54	0.03	1.47	0.43	<2	0.6		0.21			
Cs	585	97	181	68	1203	556	385	54	555	43	664	86	211	35	<21	<9		4.3	0.3	<10		10	<2		<16			
Ba	929	156	663	38	848	152	913	98	736	63	812	68	410	72	<56	<19		<11		<19		<12	1.3		<33			
La	657	78	510	49	653	123	572	51	531	12	569	71	327	40	3.0	2.1	0.6	2.4	0.3	5.96	0.52	7	2.3	0.3	2	0	0	
Ce	643	51	487	43	647	111	547	59	496	22	534	73	298	31	7.8	3.8	0.3	4.1	0.8	8.69	0.65	13	4.0	0.2	4	1	1	
Nd	611	63	465	22	603	111	489	67	471	7	484	50	298	28	23	10.4	1.7	11	1	22	5.9	24	9.6	0.5	10	1	1	
Sm	905	102	719	30	902	168	742	93	647	11	732	84	487	68	42	29	2	29	2	63	5.8	65	28	1	26	3	3	
Eu	1129	108	909	37	1140	218	891	102	804	19	931	120	589	91	70	46	4	45	4	89	3.9	94	42	0	40	5	5	
Gd	969	113	792	24	995	194	716	60	622	21	800	90	490	30	82	47	1	48	7	101	1.9	94	46	1	42	8	8	
Dy	1029	106	947	39	1147	214	697	61	556	14	918	113	596	39	133	80	4	76	5	163	18.7	141	77	2	72	12	12	
Er	769	71	811	36	981	185	441	58	348	8	787	107	521	48	130	86	9	76	8	159	49.3	113	79	3	78	10	10	
Yb	772	74	973	53	1122	185	392	36	316	14	897	120	617	65	141	114	10	94	7	205	97.3	154	99	5	96	13	13	
Lu	563	48	784	38	868	144	279	30	252	11	733	90	502	29	129	95	7	78	4	186	98.4	140	87	3	85	10	10	
Hf	368	39	377	21	473	73	213	27	219	12	431	68	228	16	70	38	7	83	17	73	2.1	45	66	3	14	1	1	
Ta	334	49	334	17	443	66	231	34	387	20	411	71	203	5	<1	0.4	0.1	0.82	0.20	1.2	0.1	1.83	0.8	0.1	0.31			
Re	0.41	0.03	1.0	0.2	<0.3		27	3	3.9	0.2	<0.2		49	7	<4	<2		<0.5		<0.9		<0.58	<0.2		0.9	0.2	0.2	
Pb	3075	235	4682	348	2168	183	10	2	578	22	2678	352	26	7	82	64	6	29	5	<3		14	41.2	2.1	<5			
Th	700	74	595	33	723	94	519	48	685	28	742	127	389	26	1.1	0.7	0.6	0.65	0.16	1.7	0.5	2.43	0.6	0.2	0.7	0.4	0.4	
U	715	91	601	32	736	99	575	56	712	22	764	144	407	33	<1	0.6	0.4	0.61	0.16	2.1	1.7	2.11	0.8	0.2	0.4	0.2	0.2	

Trace element concentrations are reported in ppm ($\mu\text{g g}^{-1}$) and the uncertainties are one standard deviation with respect to the mean. *n* is the number of analyses and 6/5, for example, should be read as 6 spots analyzed and data of 5 spots used for determining the average concentration reported here.

Table 8

Trace element compositions of garnets and magnesites.

Run no.	M318		M321		M335		M319		M318		M321		M335	
P (GPa)	6.6		6.6		8.6		6.6		6.6		6.6		8.6	
T (°C)	1285		1320		1470		1265		1285		1320		1470	
Phase	Garnet		Garnet		Garnet		Mst		Mst		Mst		Mst	
N	2/2		3/3		6/4		2/1		2/1		3/3		2/1	
	Mean	1 σ	Mean	1 σ	Mean	1 σ	Mean	1 σ	Mean	1 σ	Mean	1 σ	Mean	1 σ
Sc	467	48	637	46	799	80	25	35	40	5	28	8		
Ti	2879	147	3174	1195	6111	914	<125	94	49	6	96			
Cr	5103	560	11,500	0	15,200	0	125	252	198	50	324	70		
Mn	876	143	1451	258	1251	156	703	747	913	227	746	56		
Co	16	9	<99		152	18	82	59	55	9	158	21		
Ni	<350		<5572		<4997		<600	<336	54	15	<399			
Rb	<18		<310		<169		<30	19	3.0	2.4	<23			
Sr	<52		<841		<476		<58	50	6.2	0.2	<54			
Y	181	8	244	14	279	54	16	25	19	3	9	3		
Zr	104	8	148	6	200	47	<4	3	0.4	0.3	3.1			
Nb	4.0		<14		<10		<2	1	0.4	0.3	<1			
Cs	<5		<59		<54		21	6	2.1	2.1	<7			
Ba	<8		<113		<109		<13	17	1.5		<11			
La	4.0		<7		13		1	7	0.9	0.5	1.0			
Ce	2.1	2.5	<4		4		2	5	1.4	0.5	1.0			
Nd	3.5	3.0	<24		<16		5	6	2.6	0.1	1.0			
Sm	20	6	33		55	17	24	11	7.7	0.8	3.4	0.3		
Eu	41	4	58	13	99	18	16	24	13	2	5.4	2.1		
Gd	70	10	105	17	126	29	15	23	16	2	8	2		
Dy	288	24	356	43	544	103	38	43	35	6	17	6		
Er	607	31	752	70	1067	188	78	66	51	8	27	13		
Yb	1429	59	1682	153	2133	466	113	138	93	13	52	21		
Lu	1560	63	1950	147	2315	475	99	115	98	14	56	22		
Hf	132	13	230	47	322	74	0.43	4	0.3	0.3	3.1			
Ta	2.4	1.8	3	2	8	2	<0.3	1	0.2	0.3	0.5			
Re	1.1		11		19	4	<0.8	<0.45	<0.04		0.7			
Pb	13	16	35		<17		9	38	9.0	3.4	<2			
Th	3.2	4.0	3.8		7	4	0.2	7	0.4	0.5	0.6	0.7		
U	3.5	3.7	4.3	1.1	9	6	0.4	2	0.5	0.6	0.6	0.7		

Trace element concentrations are reported in ppm ($\mu\text{g g}^{-1}$) and the uncertainties are one standard deviation with respect to the mean. n is the number of analyses and 6/4, for example should be read as 6 spots analyzed and data of 4 spots used for determining the average concentration reported here.

non-weighted Levenberg–Marquardt fit. We focus on the three experiments that show minimum Fe-loss to the capsule (M328, M341, and M335; Fig. 6). Fitted $E_{M2(3+)}$ values for both the experiments at 6.6 GPa (M328 and M341) are essentially the same (224 GPa), but owing to slightly higher D values for HREEs in experiment M341, the fitted D_0 is somewhat higher (1.67) with respect to that in experiment M328 (0.87). The chief difference for the experiment at 8.6 GPa (M335) is lower D_0 (0.17) for incorporation of 3+ cations in the cpx M2 sites.

5.1.2. Lattice strain model for garnet–carbonate melt partitioning

The lattice-strain model was applied to 3+ cations (REEs, Y, and Sc) in the dodecahedral X-site of garnet. Although we focus on the run M335, which shows the least Fe-loss, the fitted parameters r_0 , E_X , and D_0 were obtained for all the runs (M335, M321, and M318; Fig. 7) with available trace element analyses for coexisting garnet–melt pairs. The fitted r_0 values range from 0.905 (M335) to 0.909–0.911 (M321 and M318). The predicted r_0 value, based on the model of Draper and van Westrenen (2007) and van Westrenen and Draper (2007), for the run M335 (0.909 ± 0.001 = nominal value of 0.909 with 1 σ uncertainty of 0.001) is slightly higher than our fitted values but those of M321 (0.909 ± 0.001) and M318 (0.908 ± 0.001) compare well with our fitted values within the analytical uncertainty. The average fitted Young's modulus E_X for our garnet/melt pairs are 577 ± 16 for the run M335 and 738 for the runs M321 and M318, which are broadly in agreement with the predicted values of 666 ± 50 (Draper and van Westrenen, 2007; van Westrenen and Draper, 2007). Our fitted values also compare well with the previously determined E_X values for low-Ca garnet/anhedral silicate melt pairs (van Westrenen et al., 1999, 2000). Fitted D_0 values

for our experiments vary between 4 and 6 for the experiments at 6.6 GPa (M321 and M318) and 10 for the experiment at 8.6 GPa (M335) and are lower by a factor ~3–10 with respect to the predicted values of Draper and van Westrenen (2007) and van Westrenen and Draper (2007). The lower fitted values of D_0 for our experiments may be owing to the composition of the equilibrium melt, which is very low in silica and largely an ionic liquid (Hirschmann and Ghiorso, 1994).

5.2. Bulk partition coefficients relevant for carbonate melt generation from partial melting of peridotite beneath oceanic ridges and islands

In this section we estimate bulk partition coefficients relevant for carbonatite generation at deep upper mantle conditions (Table 10, Fig. 8).

Calculation of meaningful bulk D s requires mineral modes in the lithology of interest. Based on near-solidus phase equilibria experiments of carbonated lherzolite applicable to depths of 200–300 km in the sub-oceanic mantle (Dasgupta and Hirschmann, 2006), we calculate bulk D s assuming that garnet lherzolite at depths of 200–300 km consists of 61 wt.% olivine, 5 wt.% opx, 18 wt.% cpx, and 16 wt.% garnet. Importantly, the mass proportion of orthopyroxene does not exceed more than 5 wt.% and the garnet mode is large. Both of these features are well-documented from subsolidus and near-solidus experiments (Irifune and Isshiki, 1998; Dasgupta and Hirschmann, 2006). Note that the mode we apply to trace element partitioning calculations ignores magnesite, as this phase is only 0.02–0.2 wt.% of the rock at the solidus of carbonated lherzolite with 100–1000 ppm CO_2 (Dasgupta and Hirschmann, 2006) and thus has negligible influence on bulk partition coefficients.

Table 9
Mineral-melt partition coefficients.

Run no.	M319		M312		M318		M341		M328		M321		M335		M318		M321		M335		M319		M318		M321		M335				
	Cpx		Cpx		Cpx		Cpx		Cpx		Cpx		Cpx		Garnet		Garnet		Garnet		Mst		Mst		Mst		Mst				
	Mean	1 σ	Mean	1 σ	Mean	1 σ	Mean	1 σ	Mean	1 σ	Mean	1 σ	Mean	1 σ	Mean	1 σ	Mean	1 σ	Mean	1 σ	Mean	1 σ	Mean	1 σ	Mean	1 σ	Mean	1 σ	Mean	1 σ	
Si	19.2	2.1	11.2	0.6	14.4	1.4	18.0	1.2	14.4	0.6	13.2	2.1	7.3	0.5	11.3	1.1	10.4	1.5	5.7	0.5	0.0	0.0	0.0	0.0	0.0	0.0	0.0	0.0	0.0	0.0	
Ti _m	0.23	0.02	0.12	0.02	0.21	0.05	0.21	0.04	0.25	0.02	0.18	0.04	0.14	0.03	0.30	0.04	0.35	0.05	0.66	0.08	0.0	0.0	0.0	0.0	0.0	0.0	0.0	0.0	0.0	0.0	
Al	11.0	2.2	4.9	0.4	8.3	1.4	6.5	1.1	10.6	1.7	7.7	1.5	4.9	0.5	37.8	2.9	42.0	6.1	45.0	4.0	0.1	0.1	0.0	0.0	0.1	0.0	0.0	0.0	0.0	0.0	
Cr	25.0	22.3	11.9	10.8	22	16	10.9	6.2	15.6	7.0	30.5	20.3	14.6	10.2	54.6	38.2	75.4	51.1	50.6	37.0	0.5	0.8	0.4	0.5	0.8	0.7	1.4	1.1	0.0	0.0	
Fe	1.0	0.2	0.7	0.1	1.2	0.9	0.5	0.0	0.5	0.0	1.4	0.4	0.7	0.0	4.8	0.9	3.7	0.5	1.2	0.1	1.9	0.3	2.6	0.5	1.8	0.4	0.9	0.0	0.0	0.0	
Mn	1.1	0.9	0.7	0.3	1.2	0.8	0.3	0.1	0.3	0.2	0.7	0.4	0.8	0.4	2.8	1.5	1.3	0.4	1.3	0.4	2.1	1.5	1.9	1.0	1.2	0.3	1.0	0.3	0.0	0.0	
Mg	1.32	0.05	1.26	0.08	1.29	0.17	1.19	0.02	1.19	0.02	1.30	0.12	1.10	0.02	1.76	0.04	1.63	0.04	1.18	0.02	2.9	0.1	2.9	0.0	2.7	0.1	2.2	0.0	0.0	0.0	
Ca	0.60	0.02	0.59	0.03	0.55	0.06	0.73	0.02	0.71	0.01	0.53	0.05	0.69	0.02	0.13	0.02	0.13	0.00	0.20	0.01	0.3	0.0	0.3	0.0	0.2	0.0	0.2	0.0	0.0	0.0	
Na	0.5	0.1	0.7	0.1	0.5	0.1	0.2	0.0	0.2	0.0	0.6	0.1	0.6	0.1	0.1	0.0	0.04	0.02	0.04	0.01	0.0	0.0	0.0	0.0	0.0	0.0	0.0	0.0	0.0	0.0	
Sc	1.38	0.11	0.85	0.04	1.12	0.12	2.81	0.49	1.39	0.06	0.98	0.13	0.70	0.10	3.26	0.44	4.49	0.58	8.35	0.79	0.26	0.02	0.24	0.03	0.28	0.05	0.29	0.07	0.0	0.0	
Ti	0.18	0.02	0.12	0.01	0.21	0.04	0.49	0.07	0.25	0.01	0.16	0.02	0.14	0.02	0.27	0.05	0.29	0.11	1.21	0.18			0.01	0.00	0.004	0.001	0.019	0.001	0.0	0.0	
Cr	12.9	1.9	14.35	2.58	13.93	3.01	34.39	10.07	14.2	0.3	9.8	1.5	10	2	15.51	3.02	38	4	63	7	0.65	0.09	0.76	0.13	0.65	0.16	1.3	0.3	0.0	0.0	
Mn	0.49	0.04	0.71	0.12	0.41	0.04	0.65	0.17	0.42	0.01	0.43	0.05	0.66	0.15	1.12	0.21	1.70	0.34	1.77	0.34	0.93	0.08	0.96	0.10	1.07	0.29	1.05	0.18	0.0	0.0	
Co	1.19	0.12	0.96	0.13	0.77	0.13	0.95	0.20	0.69	0.02	0.90	0.09	0.95	0.20	1.19	0.56			1.78	0.23	1.99	0.21	4.40	0.43	2.32	0.33	1.9	0.3	0.0	0.0	
Ni																															
Rb					0.013	0.006																		0.017	0.005	0.004	0.003				
Sr					0.027	0.004			0.19	0.01	0.033	0.003											0.085	0.013	0.012	0.001					
Y	0.13	0.01	0.09	0.01	0.076	0.014	0.27	0.06	0.26	0.01	0.086	0.011	0.13	0.03	0.45	0.08	0.66	0.08	1.34	0.21	0.05	0.00	0.063	0.010	0.053	0.009	0.043	0.012	0.0	0.0	
Zr	0.04	0.01	0.03	0.00	0.059	0.012	0.12	0.04	0.08	0.00	0.047	0.006	0.024	0.002	0.23	0.04	0.33	0.05	1.06	0.22			0.006	0.001	0.001	0.001	0.017	0.001	0.0	0.0	
Nb			0.001	0.001	0.001	0.000	0.0045	0.0013			0.001	0.000	0.001	0.000	0.01	0.00							0.002	0.000	0.001	0.001					
Cs					0.004	0.002			0.02	0.00											0.04	0.00	0.005	0.003	0.003	0.003					
Ba											0.002	0.000											0.020	0.003	0.002	0.000					
La	0.005	0.000	0.004	0.001	0.004	0.001	0.010	0.001	0.01	0.00	0.004	0.001	0.006	0.001	0.006	0.001			0.039	0.004	0.00	0.00	0.011	0.002	0.002	0.001	0.0032	0.0003	0.0	0.0	
Ce	0.012	0.001	0.01	0.00	0.006	0.001	0.016	0.002	0.03	0.00	0.007	0.001	0.012	0.002	0.003	0.004			0.015	0.001	0.00	0.00	0.008	0.001	0.003	0.001	0.0035	0.0003	0.0	0.0	
Nd	0.038	0.003	0.02	0.00	0.018	0.003	0.045	0.012	0.05	0.00	0.020	0.002	0.033	0.005	0.006	0.004					0.01	0.00	0.010	0.002	0.005	0.001	0.003	0.000	0.0	0.0	
Sm	0.046	0.004	0.04	0.00	0.032	0.006	0.09	0.01	0.1	0.0	0.039	0.004	0.053	0.009	0.022	0.007	0.045	0.005	0.112	0.033	0.03	0.00	0.012	0.002	0.011	0.001	0.007	0.001	0.0	0.0	
Eu	0.062	0.005	0.05	0.00	0.039	0.008	0.10	0.01	0.1	0.0	0.05	0.00	0.07	0.01	0.036	0.006	0.06	0.01	0.17	0.03	0.01	0.00	0.021	0.003	0.01	0.00	0.009	0.003	0.0	0.0	
Gd	0.085	0.008	0.06	0.00	0.048	0.010	0.14	0.01	0.2	0.0	0.06	0.01	0.09	0.02	0.070	0.013	0.13	0.02	0.26	0.05	0.02	0.00	0.023	0.004	0.02	0.00	0.016	0.003	0.0	0.0	
Dy	0.13	0.01	0.08	0.00	0.07	0.01	0.23	0.03	0.3	0.0	0.08	0.01	0.12	0.02	0.25	0.04	0.39	0.06	0.91	0.16	0.04	0.00	0.04	0.01	0.04	0.01	0.028	0.008	0.0	0.0	
Er	0.17	0.01	0.11	0.01	0.08	0.01	0.36	0.11	0.3	0.0	0.10	0.01	0.15	0.02	0.62	0.10	0.96	0.13	2.05	0.34	0.10	0.01	0.07	0.01	0.06	0.01	0.052	0.020	0.0	0.0	
Yb	0.18	0.01	0.12	0.01	0.08	0.01	0.52	0.22	0.5	0.0	0.11	0.01	0.16	0.02	1.27	0.18	1.88	0.27	3.5	0.7	0.15	0.01	0.12	0.02	0.10	0.02	0.084	0.030	0.0	0.0	
Lu	0.23	0.02	0.12	0.01	0.09	0.01	0.67	0.31	0.6	0.0	0.12	0.01	0.17	0.02	1.80	0.24	2.66	0.30	4.6	0.9	0.18	0.01	0.13	0.02	0.13	0.02	0.11	0.03	0.0	0.0	
Hf	0.19	0.02	0.10	0.02	0.18	0.04	0.34	0.04	0.20	0.01	0.15	0.02	0.063	0.006	0.28	0.04	0.53	0.12	1.41	0.30	0.001	0.000	0.008	0.001	0.0008	0.0006	0.014	0.001	0.0	0.0	
Ta			0.001	0.000	0.002	0.000	0.0051	0.0007	0.005	0.000	0.0018	0.0004	0.002	0.000	0.006	0.004	0.0071	0.0035	0.041	0.008			0.003	0.000	0.0006	0.0006	0.0025	0.0001	0.0	0.0	
Re													0.018	0.004					0.39	0.07							0.0136	0.0016	0.0	0.0	
Pb	0.027	0.002	0.01	0.00	0.013	0.002			0.02	0.00	0.02	0.00			0.006	0.006	0.01	0.00			0.0028	0.0002	0.017	0.00					0.0	0.0	
Th	0.0016	0.0001	0.001	0.001	0.001	0.000	0.003	0.001	0.004	0.000	0.0009	0.0003	0.002	0.001	0.004	0.005	0.0051	0.0007	0.017	0.008	0.0003	0.0000	0.010	0.00	0.0006	0.0005	0.0016	0.0014	0.0	0.0	
U			0.001	0.000	0.001	0.000	0.004	0.002	0.003	0.000	0.0010	0.0003	0.001	0.000	0.005	0.004	0.0056	0.0015	0.023	0.012	0.0005	0.0000	0.003	0.00	0.0007	0.0006	0.0016	0.0014	0.0	0.0	

Uncertainties are reported as one standard deviation with respect to the average and are calculated by propagating uncertainty of the individual phases. Ti_m indicates partition coefficients based on microprobe measurements.

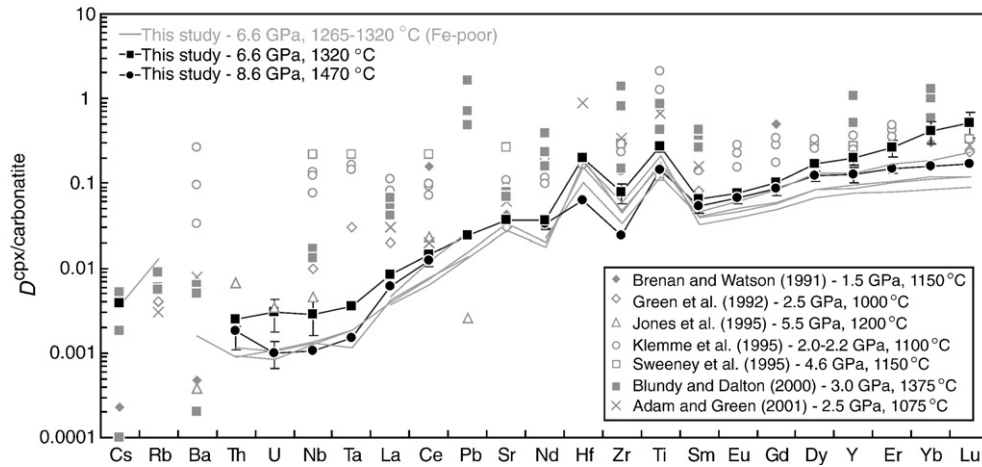


Fig. 4. Comparison between clinopyroxene/carbonatitic melt trace element partition coefficients determined in this study at 6.6–8.6 GPa with previous determinations at lower pressures (1.5–5.5 GPa). The data for 6.6 GPa are condensed to one trend, based on experiments M341 (1310 °C), M321 (1320 °C) and M328 (1320 °C).

Compared to the sub-ridge mantle, mantle upwelling beneath ocean islands has a higher mantle potential temperature (Putirka, 2005; Courtier et al., 2007; Herzberg et al., 2007; Putirka et al., 2007) and so initial generation of carbonatitic melt can occur at a greater depth. A reasonable extrapolation of the carbonated peridotite solidus (Dasgupta and Hirschmann, 2006) indicates a possible intersection with the plume adiabat (mantle potential temperature of 1500–1600 °C) at 12–14 GPa or a depth of ~300–400 km (Fig. 1), significantly deeper than the intersection beneath the sub-ridge mantle. The bulk partition coefficients prevailing during carbonate melt generation in plumes may be distinct from sub-ridge mantle, owing chiefly to stabilization of majoritic garnet and secondarily to the probable absence of orthopyroxene (Irfune and Isshiki, 1998).

Compared to the bulk lherzolite–silicate melt partition coefficients applicable to garnet or spinel-bearing basalt source regions (Salters and Longhi, 1999; Salters et al., 2002; Kelemen et al., 2003; Workman and Hart, 2005), the $D^{\text{peridotite/cbl}}$, at the near solidus condition, are larger for Cs, Rb, Ba, and for high-field strength elements including Nb, Hf, Zr, and Ti. The increased compatibility of the alkali and alkali earth elements is due chiefly to the enhanced mode of garnet and cpx and decreased mode of opx at the higher pressures where the carbonatite partial melts form. Larger values for $D^{\text{peridotite/cbl}}$ for Nb, Hf, Zr, and Ti are the result of well-known low solubility of HFSEs in ionic carbonate liquid

(Chakhmouradian, 2006) and has been experimentally observed at low pressures (Sweeney et al., 1992; Adam and Green, 2001).

5.3. Erupted carbonatite versus mantle carbonatite derived from garnet–lherzolite?

The newly estimated bulk partition coefficients allow calculation of the trace element concentrations in carbonatitic melt derived near the solidus of carbonated garnet lherzolite (Fig. 9). At very low melt fractions (0.03%) appropriate for a partial melt derived from a garnet lherzolite source with a DMM-like trace element abundance (Workman and Hart, 2005) and with 100 ppm CO₂, the melt has trace element concentrations ~100–1000 times those of chondrite source (McDonough and Sun, 1995). Compared to natural calcio- and magnesio-carbonatites from oceanic provinces such as the Canary and Cape Verde islands (Hoernle et al., 2002) and from the continents (Nelson et al., 1988), which have incompatible element concentrations that are ~1000–10,000× chondritic (Fig. 9), the calculated melt is not as enriched in Ba, Th, U, Nb, La, Ce, Sr, Nd, and HREEs. Derivation from a primitive mantle source (McDonough and Sun, 1995) results in LREE, U, Th, and Ba concentrations ~1000× chondrite for the low-degree (0.03%) carbonatitic melt. However, the calculated partial melts continue to have HREE concentrations 10 to 100 times lower than natural carbonatites (Fig. 9).

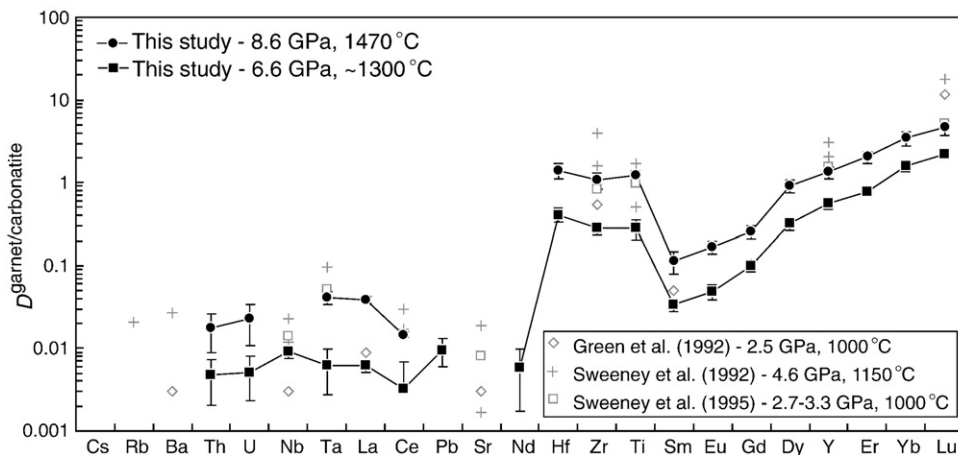


Fig. 5. Comparison between garnet/carbonatite trace element partition coefficients determined in this study at 6.6–8.6 GPa and those previously determined at lower pressures (2.5–4.6 GPa). For clarity, the data for 6.6 GPa are condensed to one trend, based on the runs M318 (1285 °C) and M321 (1320 °C).

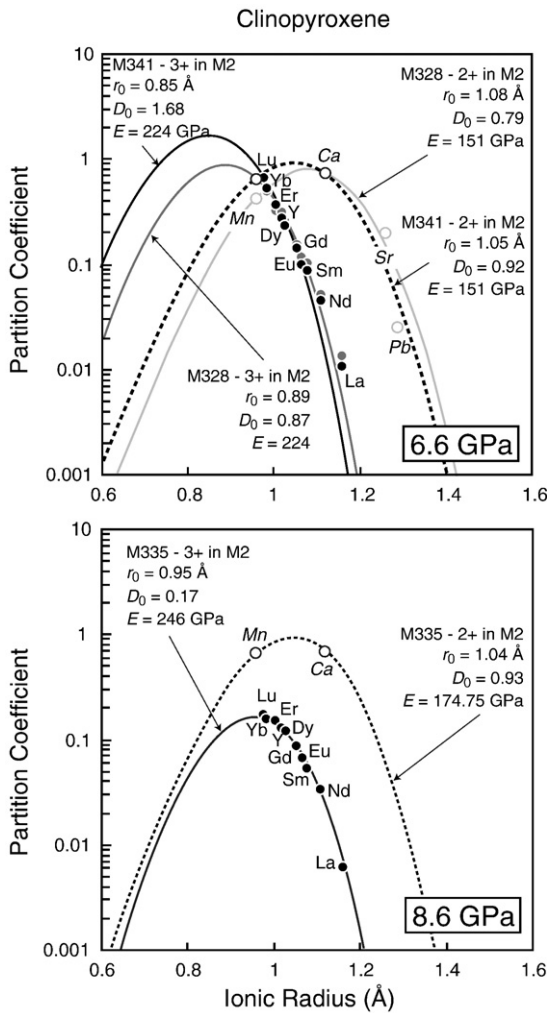


Fig. 6. Plots of D versus ionic radius for 2+ and 3+ cations incorporated into the M2 site of clinopyroxene. Best-fit parabolas are calculated following the lattice strain model of Blundy and Wood (1994, 2003) and the VIII-fold coordinated ionic radii are from Shannon (1976). 2+ and 3+ cations in the M2 site follow well-known near-parabolic trend for experiments at both 6.6 and 8.6 GPa.

Importantly, the calculated near-solidus, primary carbonatite compositions do not show key fractionations between incompatible elements that are evident in erupted carbonatites. For example, Nb/Ta ratios for the natural carbonatites are ~25–100 (Nelson et al., 1988; Hoernle et al., 2002; Chakhmouradian, 2006), whereas the melt compositions calculated from our measured partition coefficients do not show any appreciable enrichment of Nb over Ta (Fig. 9). Similarly, natural carbonatites have high Zr/Hf and Zr/Ti ratios that are not evident in the calculated partial melts (Fig. 9). Differences between calculated primary carbonate melt compositions and natural erupted magnesio-calcio carbonatites indicate that erupted carbonatites cannot simply be very small degree partial melts of normal mantle sources as previously proposed by Nelson et al. (1988). They must derive from source regions with distinct compositions and/or mineralogies and/or they must have undergone severe compositional evolution subsequent to partial melting, including fractionation of accessory phases and liquid immiscibility. For example, low pressure fractionation of apatite (Klemme and Dalpé, 2003) and baddeleyite (Klemme and Meyer, 2003) are plausible mechanisms to cause enrichment of Nb over Ta in carbonatite.

Another process that may account for the observed compositional features of erupted carbonatites is melt–rock reaction during transit through the mantle. A detailed calculation of this sort is beyond the scope of the present contribution. However, using a simple model of

zone refinement, we calculated the composition of carbonatitic melt, coming from a distal lherzolite source, which reacted with overlying lherzolite (Fig. 10). These autometamorphic model calculations, where trace carbonatitic melt reacts with 3000 times lherzolite mass, show that mantle carbonatite can retain its LREE, Ba, Th, U and Nb enrichment and approach concentrations of C_0/D . Extensive melt–rock reaction with a shallower mantle can cause modest elevation of trace element concentrations in mantle carbonatite. In fact, owing to low modal abundance of garnet at lower pressures (i.e., near the onset of garnet stability at 3 GPa, where there is less than 5 wt.% garnet: Walter, 1998), melt–rock reaction involving shallower mantle peridotite elevates the HREE abundance of carbonatite substantially (Fig. 10). Moreover, melt–rock reaction leads to carbonatitic melts with trace element characteristics that approach the natural carbonatite pattern, including fractionated Zr/Ti and Zr/Hf ratios. Hence, although distinct differences in HREE concentrations and Nb/Ta ratio remain, we identify reaction of deep carbonate melt with a shallow mantle, perhaps in the absence of garnet, as a critical process for achieving the trace element distribution of natural carbonatite.

Perhaps the most important conclusion of our melt composition estimate is that carbonated melt in equilibrium with garnet peridotite is compositionally distinct from erupted carbonatite. Hence models of carbonatite metasomatism in the asthenosphere and in basalt source regions should employ carbonate melt compositions calculated from high pressure partition coefficients rather than from erupted carbonatites. Carbonatite metasomatic fluids in the lithosphere may also be more closely related to those calculated from partition coefficients, though the lithosphere may have compositional and mineralogical complexities, such as previous metasomatic influences and the presence of accessory minerals, which impart distinct fractionations to carbonatitic liquid.

5.4. Chemical differentiation of the Earth's mantle owing to extraction of small-volume carbonatitic melt

Dasgupta and Hirschmann (2006) noted that extraction of trace carbonatitic melts from the mantle can have notable effects on the residual decarbonated mantle, including fractionation of parent–daughter elements and depletion of peridotite in highly incompatible elements. Our revised bulk partition coefficients indicate that efficient extraction of deep carbonate melt may cause peridotite to lose up to 60% of some of its highly incompatible elements for melt fractions of

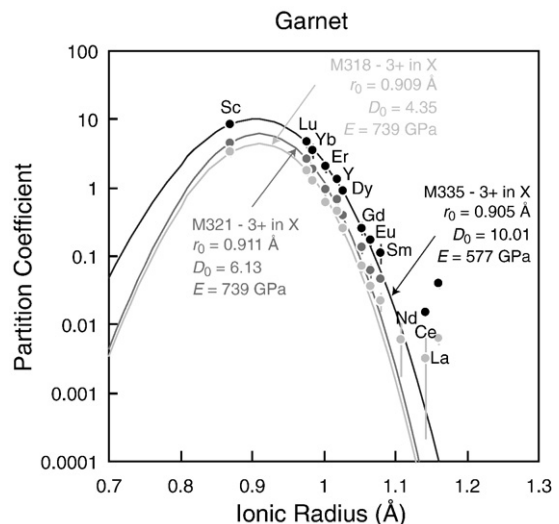


Fig. 7. Plot of D versus ionic radius for 3+ cations in garnet X-site ($X_3Y_2Z_3O_{12}$). Best-fit parabolas are following the lattice-strain model of Blundy and Wood (1994, 2003).

Table 10
Calculated bulk D s applicable for peridotite-derived carbonatite under deep upper mantle conditions.

					Mass fractions		
	$D^{cpx/cbl}$	$D^{gt/cbl}$	$D^{opx/cbl}$	$D^{ol/cbl}$	$D^{peridotite/cbl}$	$D^{peridotite/cbl}$	$D^{peridotite/cbl}$
Olivine					0.61	0.61	0.61
Opx					0.05	–	0.19
Cpx					0.18	0.20	0.17
Garnet					0.16	0.19	0.03
	$D^{cpx/cbl}$	$D^{gt/cbl}$	$D^{opx/cbl}$	$D^{ol/cbl}$	$D^{peridotite/cbl}$	$D^{peridotite/cbl}$	$D^{peridotite/cbl}$
Cs	0.017	0.0003*	0 ^s	0 ^s	0.003	0.003	0.0007
Rb	0.003*	0.013	0 ^s	0 ^s	0.004	0.003	0.001
Ba	0.008*	0.0007*	0.000001	0.000000001	0.002	0.002	0.001
Th	0.002	0.017	0.00001	0.000000001	0.003	0.004	0.001
U	0.001	0.023	0.00001	0.000000001	0.004	0.004	0.001
Nb	0.001	0.06	0.0029	0 ^s	0.010	0.012	0.003
Ta	0.002	0.041	0.0029	0 ^s	0.007	0.008	0.002
La	0.006	0.006	0.001	0.000007	0.002	0.002	0.001
Ce	0.012	0.015	0.003	0.00001	0.005	0.005	0.003
Pb	0.02	0.020	0.003	0.00001	0.007	0.008	0.005
Sr	0.03	0.008†	0.053†	0.02†	0.022	0.020	0.028
Nd	0.033	0.006	0.009	0.00007	0.007	0.008	0.008
Hf	0.063	1.41	0.17 ^s	0.036 ^s	0.268	0.303	0.107
Zr	0.024	1.06	0.17†	0.036†	0.205	0.229	0.090
Ti	0.14	1.21	0.13†	0.015	0.226	0.226	0.226
Sm	0.053	0.112	0.02	0.0007	0.029	0.032	0.017
Eu	0.07	0.17	0.03	0.00095	0.04	0.05	0.02
Gd	0.09	0.26	0.04	0.0012	0.06	0.07	0.03
Dy	0.12	0.91	0.06	0.004	0.17	0.20	0.06
Y	0.13	1.34	0.18†	0.023	0.26	0.29	0.11
Er	0.15	2.05	0.09	0.009	0.37	0.43	0.11
Yb	0.16	3.5	0.1	0.023	0.60	0.70	0.16
Lu	0.17	4.6	0.52†	0.03	0.81	0.93	0.28
Re	0.018	0.39	0	0	0.07	0.08	0.01
Sc	0.70	8.35	0.7 ^s	0.7 ^s	1.92	2.15	0.93
Cr	10	63	1.9†	1.4†	12.7	14.7	4.74
Co	0.95	1.78	2	2	1.7	1.7	1.82
Ni	3	5	4	10	7.6	7.7	7.43

Data are taken mostly from 8.6 GPa of this study; numbers in italics are taken from the 6.6 GPa experiments; †taken from Sweeney et al. (1995); *from Adam and Green (2001); ^sassumed; underlined numbers are taken from the compilation of Kelemen et al. (2003).

0.1 wt.% (Fig. 11). Also, key parent–daughter elements such as Rb–Sr, Sm–Nd, and U–Th–Pb can be fractionated in the residue and in the near solidus carbonatitic melt with respect to the unmelted source (Fig. 11). For example, removal of a 0.1% melt creates a residue for which the Rb/

Sr, U/Pb, and Th/U ratios are, respectively, 29, 12, and 6% lower and the Sm/Nd ratio is ~ 11% higher than the pristine source.

Extraction of small amounts of carbonatite may have contributed to the ongoing differentiation of the mantle through geologic time. To

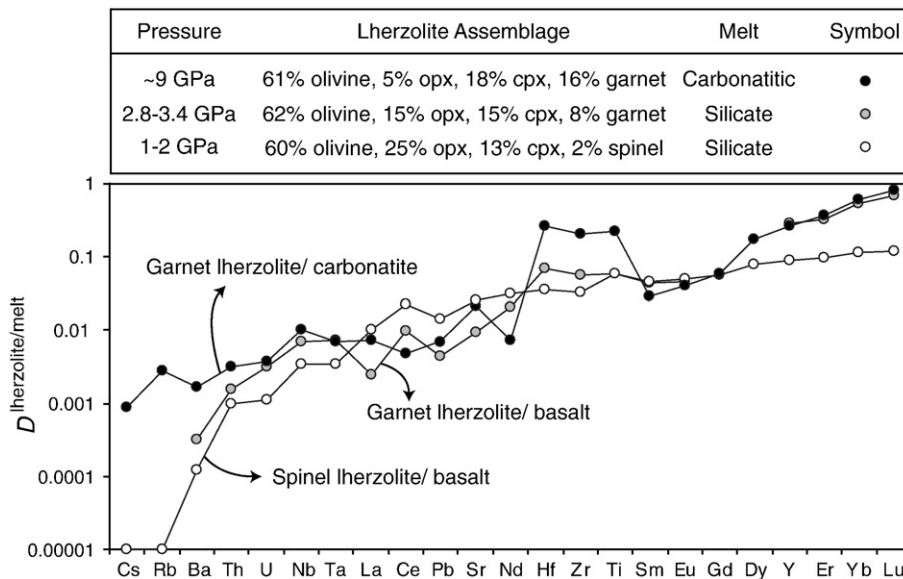


Fig. 8. Bulk partition coefficients applicable to carbonatite melt generation from garnet Iherzolite at 6–9 GPa (black symbols: this study), compared with estimates of near-solidus bulk partition coefficients between garnet- (grey symbols) and spinel-peridotite (white symbols) and basaltic melt. The $D^{gt.Iherzolite/basalt}$ is based on the data of Salters et al. (2002) and for $D^{sp.Iherzolite/basalt}$ from Workman and Hart (2005). Compared to Iherzolite-near-solidus basaltic melt bulk partition coefficients, $D^{gt.Iherzolite/cbl}$ for highly incompatible elements such as Cs, Rb, Ba, and those of HREEs are distinctly higher at deep upper mantle conditions. This is owing to higher modal abundance of garnet in the bulk rock at higher pressures. $D^{gt.Iherzolite/cbl}$ are also distinctly higher for 4+ HFSEs including Hf, Zr, and Ti, owing to low solubility of HFSEs in ionic carbonatitic liquid.

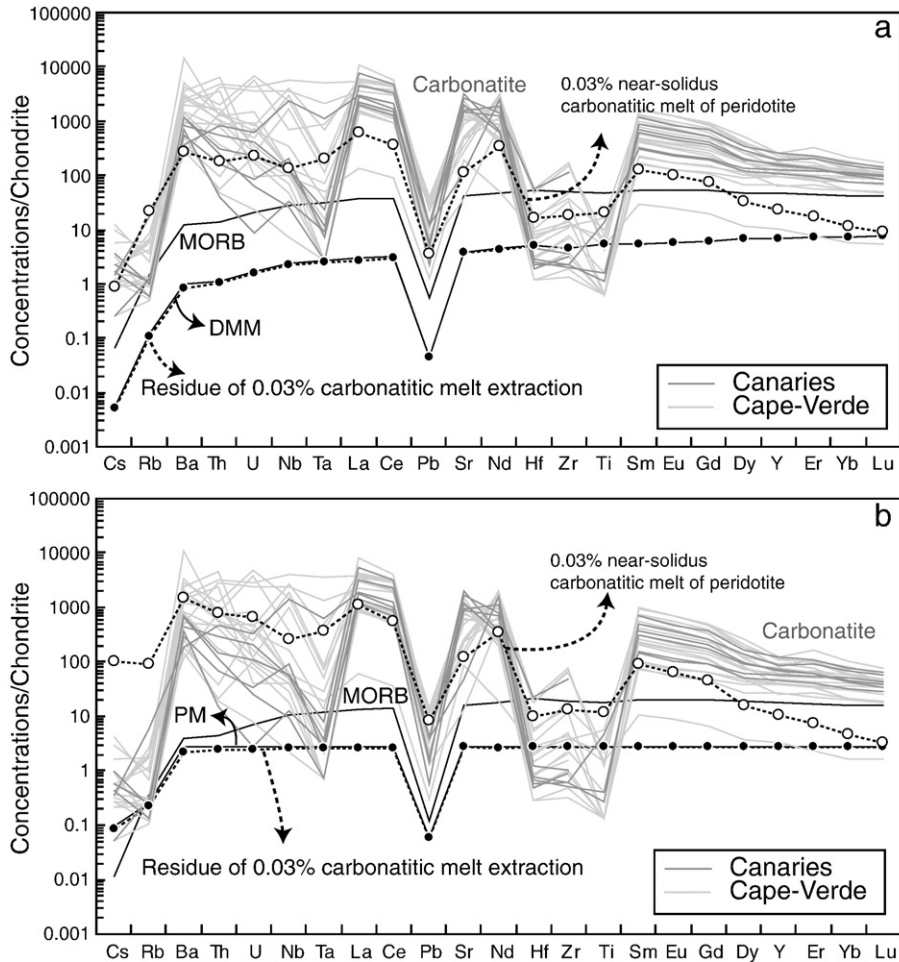


Fig. 9. Comparison between trace element patterns of natural carbonatites from oceanic domains and near-solidus carbonatitic melt composition (open circles) generated from (a) a depleted upper mantle source (DMM: Workman and Hart, 2005) (top panel) and (b) primitive mantle composition (PM: McDonough and Sun, 1995). The synthetic carbonatitic melt composition was calculated using the bulk garnet lherzolite–carbonatite partition coefficients derived in this study and using a batch melting equation and a melt fraction of 0.03%. Shown for comparison are the natural carbonatite compositions from ocean islands of Canaries (dark grey) and Cape Verde (light grey) (Hoernle et al., 2002). Continental carbonatites have similar normalized trace element patterns except for Pb (Nelson et al., 1988), but are not shown for clarity. Even at vanishingly small melt fractions, carbonatites derived from mantle compositions similar to DMM are not sufficiently enriched in highly incompatible elements to account for the trace element abundances in natural erupted carbonatites. If the source is more similar to primitive mantle, then the incompatible element enrichments of small-degree partial melts may be comparable to those of natural oceanic carbonatites, although some key differences remain, as discussed in the text. Shown for reference are the normalized patterns for MORB, the source DMM, the source primitive mantle, and the residues of DMM and primitive mantle (closed circles) after trace carbonate melt extraction.

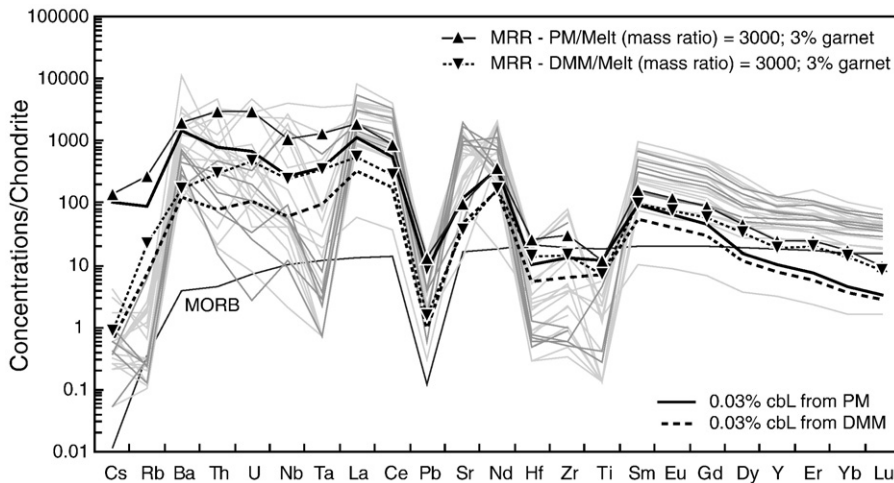


Fig. 10. Comparison between trace element patterns of natural carbonatites from oceanic domains and carbonate melts generated by small-degree partial melting followed by melt–rock reaction. Illustrated are the chondrite-normalized multi-element pattern of 0.03% carbonatite melt (cbL) generated from a depleted upper mantle source (DMM: Workman and Hart, 2005) (dashed line) and from a primitive mantle source (PM: McDonough and Sun, 1995) (solid line), as well as the calculated concentrations in melt modified by melt–rock reaction (upright and inverted triangles). The melt–rock reaction (MRR) calculations assume a constant melt mass, a rock/melt ratio of 3000, and a peridotite mineral assemblage with 61% olivine, 19% opx, 17% cpx, and 3% garnet. The calculation indicates that deep carbonate melt can retain its elemental abundance by reacting with a large mass of peridotite as it approaches a concentration of C_0/D . However, this zone refinement process fails to elevate the elemental concentration to match those of the erupted carbonatites. Carbonatite symbols are same as in Fig. 9.

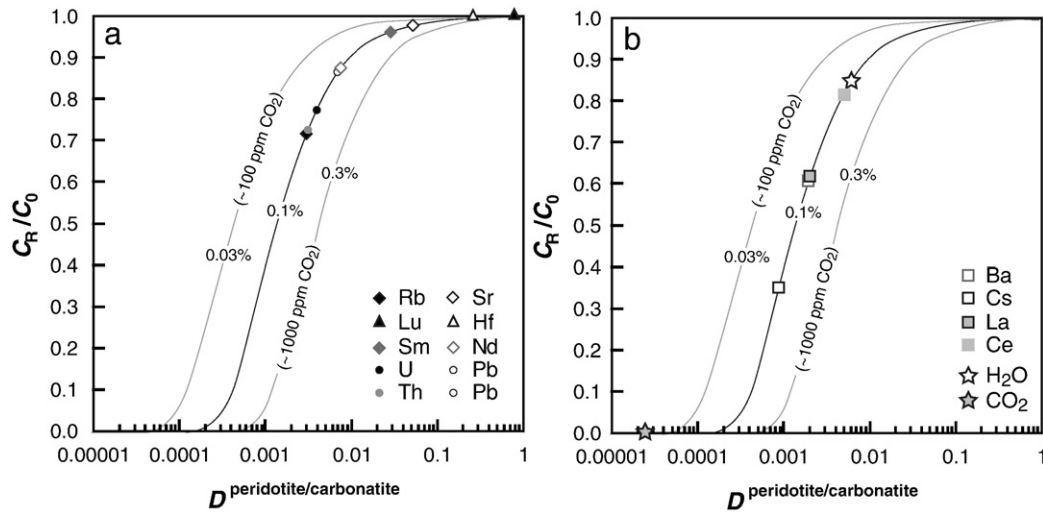


Fig. 11. Predicted depletion and fractionation of various trace elements in the source peridotite, owing to fractional extraction of trace carbonatitic melt, based on the partition coefficients measured in this study. The source depletion curves as a function of bulk partition coefficients are shown for melt fractions of 0.03%, 0.1%, and 0.3%, but the elements are arbitrarily arranged along the curve with melt fraction of 0.1%. (a) Fractionation between radiogenic parent (solid symbols) and daughter (open symbols) elements in the source peridotite, owing to fractional extraction of 0.1% carbonate melt. Deep carbonate melt extraction likely makes the source peridotite enriched in Sm/Nd and depleted in U/Pb, Th/Pb, and Rb/Sr. (b) Depletion of highly incompatible tracers and volatiles owing to fractional extraction of 0.1% carbonatite melt. Up to 40% depletion of source peridotite is expected for elements such as Ba and La.

illustrate the general sense of the isotopic evolution that may result, we have calculated the compositions of two hypothetical complementary reservoirs resulting from extraction of a small fraction (0.1%) carbonatite melt from a primitive mantle (PM) 2 Ga in the past. The isotopic composition of the resulting residue and enriched (purely carbonate) reservoirs are given in Table 11 and illustrated in Fig. 12. The carbonatite evolves to a composition with highly radiogenic $^{87}\text{Sr}/^{86}\text{Sr}$ (0.7132) and unradiogenic $^{143}\text{Nd}/^{144}\text{Nd}$ (0.51074) (Fig. 12a), and with Pb isotopes that are more radiogenic than PM but that are not extreme (Fig. 12b). Dilute contributions of this carbonatite to silicate mantle compositions, as would occur during carbonatite metasomatism, would yield less extreme isotopic compositions, and these may be similar to EM1-like mantle domains. This “flavor” of isotopic enrichment is quite distinct from HIMU, for which the Pb isotopes would be highly radiogenic and the Sr and Nd isotope ratios would be less extreme, and so our calculations do not support models in which HIMU originates from peridotite-derived carbonatite metasomatism (Kamber and Collerson, 1999). However, our analysis does not rule out genesis of HIMU linked to carbonatite metasomatism, where carbonatite derives from a recycled lithology with much higher U/Pb ratio. In fact, preferential loss of Pb and Rb over U and Sr, respectively, (Kogiso et al., 1997) and retention of carbonate (e.g., Yaxley and Green, 1994) during subduction devolatilization supports such an hypothesis. Our calculation also indicates that the Hf isotope system is little-affected by carbonatite extraction (Table 11), and confirms the previous suggestion of Bizimis et al. (2003). Finally, our partitioning data suggest significant fractionation between Sm and Nd

but no appreciable fractionation between Lu and Hf. This indicates that residues of carbonatite melt extraction and domains metasomatized by carbonatite may have composition that, if stored in the mantle for $\sim 10^8$ – 10^9 years, will develop Hf and Nd isotope ratios distinct from the prevailing Hf–Nd isotopic array. Observed instances of Hf–Nd decoupling in oceanic lithosphere (Bizimis et al., 2004), kimberlites (Nowell et al., 2004) and kimberlite-borne xenoliths (Schmitz et al., 2004) may originate in part from carbonatite–peridotite related fractionation.

5.5. Signal of deep CO_2 -rich melt in the erupted MORB

Small volumes of carbonatitic melt produced deep beneath ridges are expected to be diluted by much higher extents of silicate melting at shallower depths and this will likely diminish the influence of carbonatites on major and trace element characteristics of MORB. However, the signal of deep carbonate melting may be evident from fractionation of highly incompatible trace elements and short-lived radionuclides, which could survive shallower processes.

5.5.1. CO_2/Nb ratio of erupted MORBs

Much or all of the carbon found in erupted MORB may be initially liberated from the mantle as a carbonatitic melt at depth (Dasgupta and Hirschmann, 2006). The proportion of carbonatite that could be added to erupted MORB ranges from 0.04%, for depleted Siqueiros lavas that have 200 ppm CO_2 (Saal et al., 2002), up to 13% for the most CO_2 -rich “popping rocks” from the North Atlantic which have 5.8 wt.% CO_2 (Cartigny et al., 2008), assuming that the added melt was a carbonatite with 45 wt.% CO_2 . However, an interesting and important constraint noted by Cartigny et al. (2008) is that the CO_2/Nb ratios of the popping rocks, which range from 300 up to 1950, are greater compared to those in depleted MORBs (e.g., $\text{CO}_2/\text{Nb} = 240 \pm 40$ in Siqueiros lavas; Saal et al., 2002). Moreover, enrichments in CO_2 and CO_2/Nb in popping rocks are accompanied by enrichments in other trace element ratios, such as La/Sm (Cartigny et al., 2008) and these correlations allow exploration of the origin of the CO_2 -enrichments in the popping rocks and perhaps into the origin of CO_2 in less extreme MORB.

As noted by Cartigny et al. (2008), the observed variations in CO_2 , CO_2/Nb , and La/Sm cannot be explained by variable degrees of partial melting of a single source. The simplest hypothesis is that the extreme enrichment of the popping rocks results from addition to typical MORB

Table 11

Summary of model isotope evolution calculation.

	PM	Residue	0.1% carbonate melt
Rb/Sr	0.0302	0.0252	0.1387
Sm/Nd	0.3248	0.3589	0.0866
U/Pb	0.1353	0.1237	0.2165
Th/Pb	0.5300	0.4542	1.0599
U/Th	0.2553	0.2724	0.2043
Lu/Hf	0.2385	0.2391	0.0791
$^{87}\text{Sr}/^{86}\text{Sr}$	0.70450	0.70410	0.71323
$^{143}\text{Nd}/^{144}\text{Nd}$	0.51264	0.51291	0.51074
$^{206}\text{Pb}/^{204}\text{Pb}$	17.51	17.25	19.33
$^{207}\text{Pb}/^{204}\text{Pb}$	15.36	15.33	15.59
$^{208}\text{Pb}/^{204}\text{Pb}$	38.01	37.51	41.53
$^{176}\text{Hf}/^{177}\text{Hf}$	0.28276	0.28276	0.28189

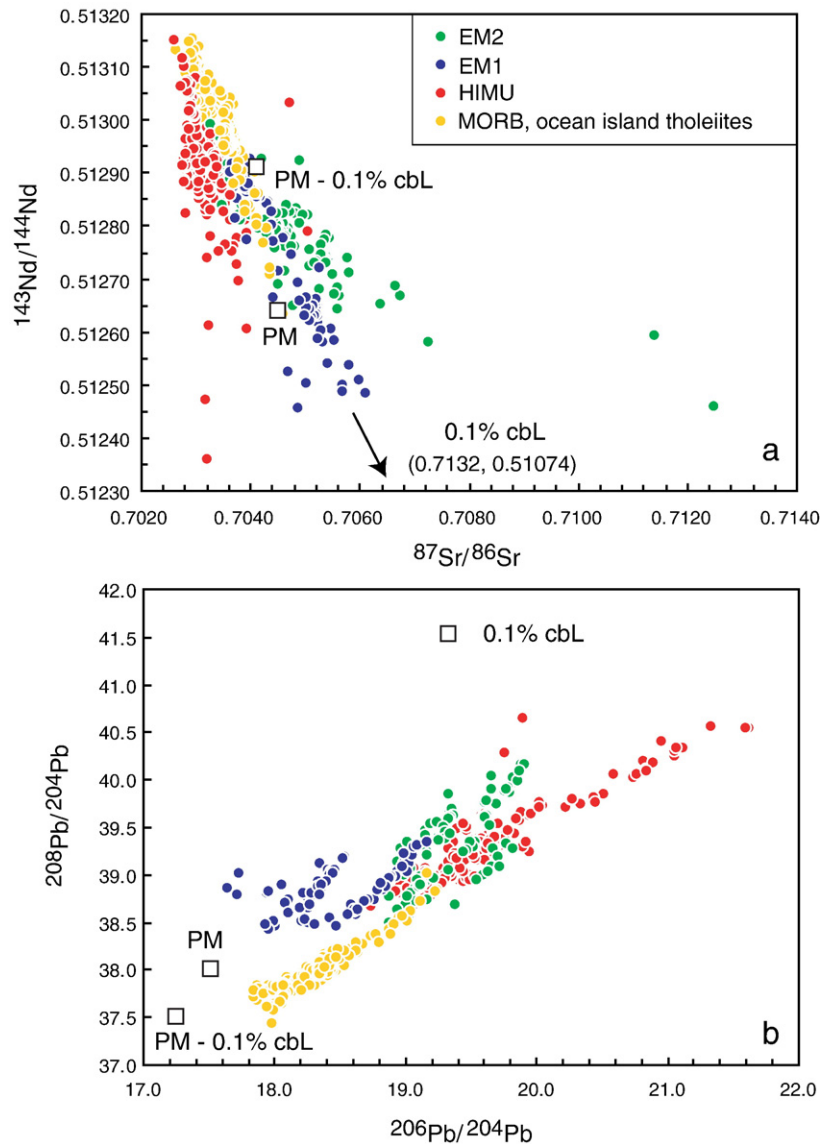


Fig. 12. Isotopic composition of primitive mantle (PM), 0.1% carbonate melt (cbL), and PM residue of such melt extraction that evolved separately for 2 Ga. Isotopic compositions of oceanic basalts with HIMU, EM1, and EM2 flavors and MORB and ocean island tholeiites are plotted for comparison from the compilation of Jackson and Dasgupta (2008). The isotopic characteristics of the carbonate melt are similar to, but more extreme than, EM1-like compositions. Addition of small amounts of such material to regions of the mantle may therefore produce domains with similarities to EM1.

of a carbonatite melt formed from deep melting of a normal MORB source. However, application of the partition coefficients determined here shows that carbonatite with ~45 wt.% CO_2 formed from very small degree (0.01–0.1%) partial melting of depleted mantle similar to DMM (Workman and Hart, 2005) at 200–300 km will have a CO_2/Nb ratio of ~30,000. Variable addition of such extraordinary composition melts to the very shallow portion of the MORB source region would have extreme influence on the CO_2/Nb ratios of MORB, whilst having only a modest effect on either absolute CO_2 concentrations or other trace element ratios. For example, addition of just 0–0.2% of such a melt to a typical depleted MORB, as from Siqueiros (100 ppm CO_2 , $\text{CO}_2/\text{Nb}=240$, 0.8 ppm La, 1.6 ppm Sm; Perfit et al., 1996; Saal et al., 2002) would span the range of CO_2/Nb ratios known for MORB (Cartigny et al., 2008) without any appreciable effect on CO_2 concentrations or La/Sm ratios (Fig. 13).

Alternatively, we may consider whether the popping rocks contain a carbonatite component that derives from a trace element-enriched source. Fig. 13 shows calculation for modest additions of carbonatite melt formed by a source with significant enrichments in La and Nb

(La = $3 \times \text{BSE}$; Nb = $10 \times \text{BSE}$). Small degree partial melts of such a source have less extreme CO_2/Nb ratios (750) and produce mixing trajectories with similarities to the $\text{CO}_2/\text{Nb}-\text{CO}_2$ and $\text{CO}_2/\text{Nb}-\text{La}/\text{Sm}$ trends defined by the popping rocks. Thus, the popping rocks could result from addition of carbonatite to a normal MORB source if the carbonatite derived from a highly enriched source.

An important consideration is that it may not be chemically feasible for carbonatites to migrate into the zone of silicate melting beneath ridges. Rather, deep carbon-rich melts ascending from depth likely evolve, as they react with surrounding mantle, from carbonatite to carbon-rich silicate melt (Dasgupta et al., 2007) to basaltic melt with comparatively dilute CO_2 concentrations. Clearly in the case of the “popping rocks” any such melts must have retained high carbon concentrations, though they would be much less CO_2 -rich than carbonatite.

We can investigate whether addition of carbonated silicate melts to normal MORB can account for the CO_2 and trace element variations in undegassed popping rocks (Cartigny et al., 2008). First we consider the case where the carbon-rich melt with 10 wt.% CO_2 derives from a deep source that is similar to normal DMM (Workman and Hart, 2005).

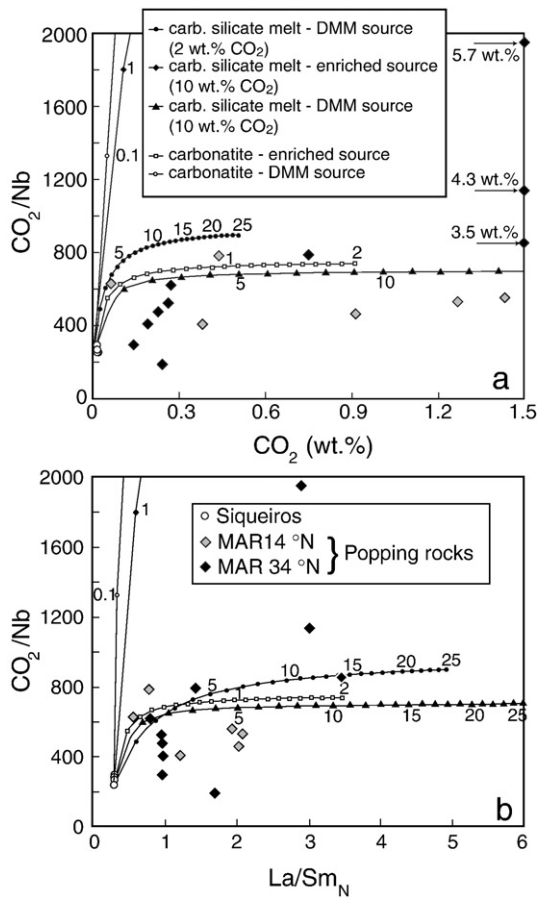


Fig. 13. CO₂/Nb versus (a) CO₂ concentration and (b) the primitive mantle-normalized La/Sm ratio for undegassed MORB, with data from Siqueiros (Saal et al., 2002) and from the North Atlantic popping rocks (Cartigny et al., 2008). The primitive mantle normalization is from McDonough and Sun (1995). The data are compared to 5 different mixing trends between normal depleted MORB (0.8 ppm La, 1.6 ppm Sm, 100 ppm CO₂, 0.4 ppm Nb) and either carbonatite or carbonated silicate melts. The carbonatitic melt compositions have 45 wt.% CO₂ and trace elements that are calculated as 0.1% partial melts from a DMM source (Workman and Hart, 2005) or an enriched source (1.33 ppm La, 0.26 ppm Sm, 6.58 ppm Nb) and $D_{Nb}^{gt.lherzolite/cbl}$, $D_{La}^{gt.lherzolite/cbl}$ and $D_{Sm}^{gt.lherzolite/cbl}$ from Table 10 (0.01, 0.002 and 0.029, respectively). The carbonated silicate melt has either 2 or 10 wt.% CO₂ and is assumed to have reacted with an effectively infinite mass of either a DMM source or an enriched source (0.253 ppm La, 0.273 ppm Sm, 0.987 ppm Nb), such that its trace element composition is given by C_0/D , with $D_{Nb}^{gt.lherzolite/basalt}$ taken from Fig. 8 ($D_{Nb}^{gt.lherzolite/basalt}$, $D_{La}^{gt.lherzolite/basalt}$ and $D_{Sm}^{gt.lherzolite/basalt}$ = 0.00691, 0.00246, and 0.0439, respectively). The ornaments and numbers along the curves indicate proportions of carbon-rich melt added in percent by mass, with carbonatite melt addition in increments of 0.1% and carbonated silicate melt in increments of 1%.

Extensive reaction between percolating melts and surrounding wall rocks leads to trace element enrichments that tend to C_0/D , where D_s are the applicable partition coefficients for silicate melts (Fig. 8). In this case, the resulting carbonated silicate melts will have much lower CO₂/Nb ratios than carbonatites and, potentially, similar or higher La/Sm ratios. In Fig. 13 we present example calculations of the effect of mixing between two carbonated silicate melts and normal depleted MORB; one with 2 wt.% CO₂ and the other with 10 wt.% CO₂. The melt with 10 wt.% CO₂ suffers from the same problem as the carbonatite derived from DMM, in that it results in extremely high CO₂/Nb without accounting for either the observed CO₂ concentrations or La/Sm. Addition of the melt with 2% CO₂ can reproduce the trend of CO₂/Nb vs. La/Sm from the undegassed MORB. However, approximately 15% addition is required to reach La/Sm ratios similar to the most enriched basalts, and such melts have merely 0.3 wt.% CO₂, far less than is observed for many of the popping rocks.

The final possibility is that the CO₂-rich agent responsible for the enrichments observed in the popping rocks is a carbonated silicate melt derived from a modestly enriched source. As shown in Fig. 13, addition of a melt with 10 wt.% CO₂ derived from a source with REE elements similar to DMM, but with modestly enriched Nb (1.5 × BSE) can produce CO₂ concentrations and CO₂/Nb ratios similar to the popping rocks trend.

In summary, deep carbonated liquids, whether carbonatitic or carbonated silicate melts, have high CO₂/Nb ratios, even when they are derived from depleted sources similar to DMM. Thus, if variable CO₂ concentrations in MORB derive from variable addition of CO₂-rich melts, we do not expect CO₂/Nb ratios to be constant. This is contrary to the supposition of Saal et al. (2002), but consistent with the observations of CO₂-enriched popping rocks (Cartigny et al., 2008). Further, the extreme enrichments in CO₂ found in the North Atlantic popping rocks (Cartigny et al., 2008) and their accompanying variations in CO₂/Nb and La/Sm, cannot be derived from addition of very small-degree melts from depleted DMM-like sources, but can be accounted for by addition of carbonatite or carbonated silicate melt derived from a Nb-enriched source. Because carbonatite should react with the upper mantle to form carbonated silicate liquid, it is probable that the latter type of melt is the key agent responsible for the observed CO₂-enrichments and CO₂/Nb variations.

5.5.2. Signal of deep-sourced CO₂-rich melt in erupted MORB—a U-series perspective

In this section we turn our attention to the ²³⁰Th, ²³¹Pa, and ²²⁶Ra excesses observed in MORB, which are typically on the order ~10–15%, ~200–300% and ~200–300%, respectively, for (²³⁰Th/²³⁸U), (²³¹Pa/²³⁵U) and (²²⁶Ra/²³⁰Th) activity ratios (Elliot and Spiegelman, 2003). We consider whether contributions from deep carbonatitic melts can account for some or all of these observed disequilibria features in MORB.

For a typical range of mantle potential temperatures beneath oceanic ridges (1300–1400 °C: Ita and Stixrude, 1992; McKenzie et al., 2005; Courtier et al., 2007; Herzberg et al., 2007), partial melting in volatile-free peridotite begins in the spinel peridotite field, where the fractionation between U and Th during partial melting may be too small to account for observed ²³⁰Th excesses in MORB (Salters et al., 2002). Therefore, it is generally thought that the observed ²³⁰Th excesses require melting from a garnet-bearing source, including perhaps of eclogite or garnet pyroxenite domains (Hirschmann and Stolper, 1996) or small amounts of dehydration melting of garnet peridotite (Hirth and Kohlstedt, 1996). Generally, carbonatites have been discounted as potential sources that can produce ²³⁰Th excesses because young erupted carbonatites from Oldoinyo Lengai have (²³⁰Th/²³⁸U) much less than unity (Pyle et al., 1991). However, the Oldoinyo Lengai natrocarbonatites have undergone extensive differentiation, potentially including considerable contributions from trace minerals with unusual partitioning behavior, and so their (²³⁰Th/²³⁸U) do not necessarily reflect processes in their mantle source. Our results suggest that $D_{Th}^{gt.lherzolite/cbl} < D_{U}^{gt.lherzolite/cbl}$ so it is plausible that a deep carbonatitic melt can contribute to observed high values of (²³⁰Th/²³⁸U) in MORB. Similarly, the comparatively high values of $D_{U}^{lherzolite/cbl}$ and $D_{Th}^{lherzolite/cbl}$, as compared to $D_{U}^{lherzolite/basalt}$ and $D_{Th}^{lherzolite/basalt}$ (Fig. 8) and suggest that such melts could also contribute to high (²³¹Pa/²³⁵U) and (²²⁶Ra/²³⁰Th) ratios of erupted MORB, assuming that $D_{Ra} \ll D_U$ and $D_{Pa} \ll D_U$. A key question, however, is whether small-degree melts generated at such great depths can segregate from the mantle on time scales that preserve disequilibrium ratios.

To explore the possible contribution of deep carbonatite melting to (²³⁰Th/²³⁸U), (²³¹Pa/²³⁵U), and (²²⁶Ra/²³⁰Th) in MORB, we calculated the (²³⁰Th/²³⁸U), (²³¹Pa/²³⁵U), and (²²⁶Ra/²³⁰Th) of aggregate melts as a function of upwelling rate, following the formalism of Spiegelman and Elliot (1993) and the UserCalc algorithm of Spiegelman (2000). The model, summarized in Fig. 14, considers a one-dimensional steady state upwelling column, where the flows of solid matrix and melt are

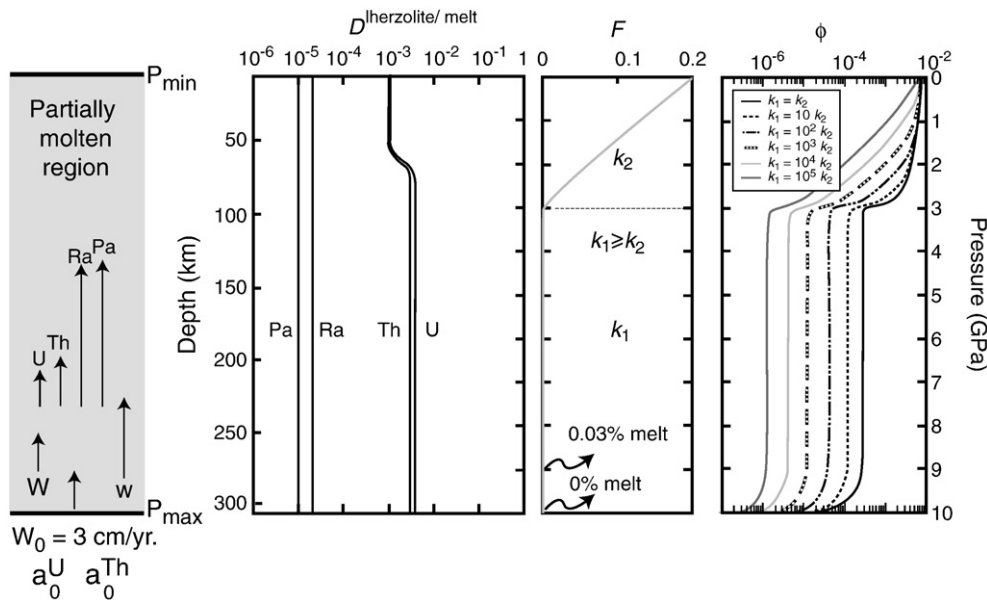


Fig. 14. Graphical illustration of the model employed for calculating U-series disequilibria in erupted MORB, after Spiegelman (2000), taking into account the contribution from trace carbonate melt generated in the deep upper mantle. The left most panel shows a steady-state, one dimensional melting column where the partially molten region extends down to a depth of ~300 km. The solid matrix and melt velocity are given by W and w , with initial matrix velocity (W_0) set to 3 cm/year. Owing to differences in partition coefficients and the resulting chromatographic separation, U, Th, Pa, and Ra have different ascent velocities (as indicated by arrows of different lengths; longer arrows indicate faster velocities) and residence times in the melting column. The lherzolite–melt partition coefficients (shown in the second panel) between ~300 km and ~70 km GPa are as determined in this study and those for spinel peridotite, between ~70 km and surface, are from Kelemen et al. (2003). Melt fraction, F , increases from 0 at ~300 km to 0.03% at ~270 km and then stays unmodified after the exhaustion of the magnesite. Further enhancement of the melt fraction occurs from ~90 to 100 km as carbonated silicate melting starts (Dasgupta et al., 2007) and then the volatile-free peridotite is crossed at ~60–70 km. The melt fraction reaches a maximum of 20% at the surface. The permeability in the bottom, carbonate melt only, layer (between 330 and 100 km or 10–3 GPa) is given by k_1 and that for the silicate melt present, top layer (3–0 GPa) by k_2 and where $k_1 \geq k_2$. The extreme right panel shows the porosity as a function of depth for a range of input permeability contrast (k_1/k_2) between the top and the bottom layer. The porosity, ϕ at the top of the column is set at 0.008.

calculated explicitly. The initial melting begins at a depth of ~300 km (Fig. 14), with 0.03% carbonatitic melt (corresponding to ~100 ppm CO_2 in the source peridotite) generated between ~300 and 270 km. After exhaustion of the carbonate phase, the melt fraction remains virtually constant until carbonated silicate melting commences at a depth of ~90 km (Dasgupta et al., 2007) and enhanced silicate melting continues as the volatile-free peridotite solidus is crossed at ~60 km (Hirschmann, 2000). The peridotitic mantle material enters the melting column in secular equilibrium, and disequilibrium is created by the difference in the residence time of U, Th, Pa, and Ra in the melt owing to the difference in partitioning behavior of the parent and daughter nuclides between the solid and the melt. Values of $D^{\text{lherzolite/cbl}}$ for U and Th between 300 and 90 km are taken to be 0.004 and 0.003 respectively, based on the present study, whereas for the silicate melting regime the applicable D s for U and Th are 0.0011 and 0.001, respectively, and are taken from the compilation of Kelemen et al. (2003) (Fig. 14). To estimate the plausible contributions of deep carbonatite to ($^{231}\text{Pa}/^{235}\text{U}$) and ($^{226}\text{Ra}/^{230}\text{Th}$) ratios, we assume that $D_{\text{Ra}}^{\text{lherzolite/melt}}$ and $D_{\text{Pa}}^{\text{lherzolite/melt}}$ are equal to 0.00001 and 0.00002, respectively, and that they do not vary with depth in the melting column. To capture the dynamics of fast-moving carbonatitic melt, we explore the possibility that effective permeability in the bottom layer (k_1 : Fig. 14) is up to 10^6 times greater than in the top layer (k_2 : Fig. 14). A much higher effective permeability in the deep, natural carbonate melt-present regime is supported by the differences in viscosity between $\text{K}_2\text{Ca}(\text{CO}_3)_2$ and $\text{K}_2\text{Mg}(\text{CO}_3)_2$ melts (10^{-3} Pa s: Dobson et al., 1996) and basalts (1–10 Pa s) (Shaw, 1972), because the relative permeability factor, k_r is proportional to the ratio of melt viscosity between the top and the bottom layer:

$$k_r = \frac{k_1}{k_2} \alpha \frac{\mu_{\text{silicate melt}}}{\mu_{\text{carbonate melt}}} \quad (2)$$

If the assumed enhancement in permeability in the bottom layer is applicable, then assuming a maximum porosity at the top of the

column of 0.008, the porosity, ϕ , at the bottom layer could be as low as $\sim 10^{-6}$ with F of 0.0003.

Resulting calculations show that carbonatitic melt, which is fast-moving relative to its source peridotite, can retain an elevated ($^{230}\text{Th}/^{238}\text{U}$) activity ratio and that erupted MORB can have 6–16% ^{230}Th -excesses for permeability factors k_1/k_2 ranging between 1 and 10^6 (Fig. 15). If the matrix velocity is between 0.5 and 5 cm/year, the porosity between 0.1 and 1%, and the permeability factor is between 10 and 10^5 , the deep carbonatite partial melts can contribute 15% ^{230}Th -excess to erupted MORB (Figs. 15 and 16). Thus, at least for slow and moderate-spreading rate ridges, it is possible that the ($^{230}\text{Th}/^{238}\text{U}$) excesses in MORB derive from deep, carbon-rich melting. It is less clear whether a similar explanation is viable for fast-spreading ridges, where upwelling velocities may approach 8 cm/year, but this question turns in part on whether such fast upwelling velocities extend to the 200–300 km depths where carbonatite formation may be occurring.

The calculations also indicate that very strong ^{231}Pa excesses may be produced by carbonatitic partial melting deep beneath oceanic ridges and that these excesses may persist in melts extracted at shallow depths (Fig. 17a). For example, for values of k_1/k_2 in the range of 100–1000, deep carbonatitic melts will have strong ^{231}Pa excesses that persist through further upwelling and melting, leading to ($^{231}\text{Pa}/^{235}\text{U}$) excesses in erupted MORB of ~2 to ~7. On the other hand, strong ^{226}Ra excesses developed by this deep melting do not persist to the surface (Fig. 17b), owing to much shorter half-life of ^{226}Ra , and so not more than 15–20% ^{226}Ra excesses could plausibly derive from deep carbonatitic melts. The rest must come from shallower processes (e.g., Jull et al., 2002).

Our model is reminiscent of the hypothesis of Faul (2001), who showed that a volumetrically small, low density, low viscosity, deep-sourced, volatile-rich melt can preserve its isotopic disequilibria because of rapid movement through porous flow. However, there are key differences between the two models. First, Faul (2001) posited melting beginning at 100–120 km, whereas carbonatite may be stable to depths as great as ~300 km. Second, carbonatitic melts may allow

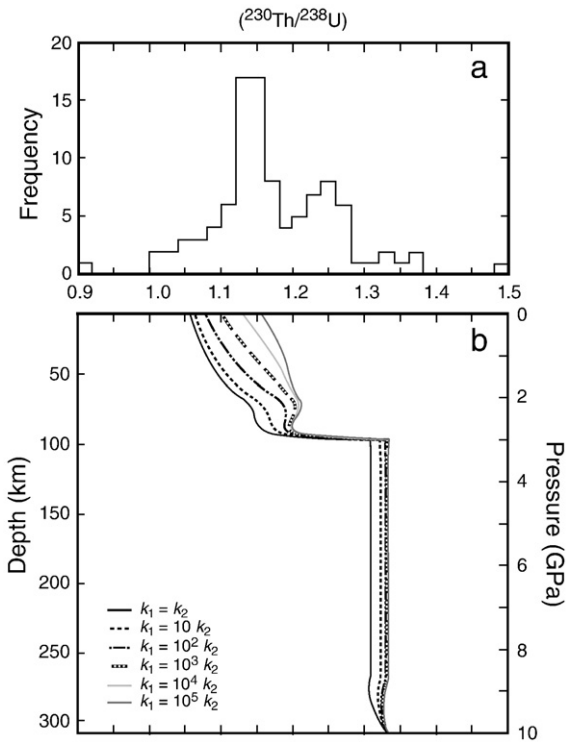


Fig. 15. (a) The frequency distribution of $(^{230}\text{Th}/^{238}\text{U})$ activity ratio observed in MORB from the compilation of Elliot and Spiegelman (2003) and (b) the depth profile of the calculated $(^{230}\text{Th}/^{238}\text{U})$ activity ratio using the model of Spiegelman and Elliot (1993) and using the model parameters presented in Fig. 14. The activity ratio at the base of the melting column is defined by $D_{\text{U}}^{\text{glt.lherzolite/cbl}}/D_{\text{Th}}^{\text{glt.lherzolite/cbl}}$ of 1.33 as determined in this study for generation of trace carbonate melt from garnet lherzolite at ~300 km depth. Very low viscosity and great connectivity at a very low melt fraction for carbonatitic melt allows many fold increase in the permeability for the bottom layer, which in turn allows a low porosity that helps retaining a high $(^{230}\text{Th}/^{238}\text{U})$ activity ratio in the aggregate partial melt. Our model shows that 10–15% ^{230}Th excesses in the erupted MORB may result from contribution of 0.03% carbonatitic melt pulse from great depth.

mobility at porosities that are substantially lower than the 0.1% assumed by Faul (2001). More generally, the model of Faul (2001) relies on a unique high-porosity structure of the upper parts of the source region that may not be realistic (Wark et al., 2003). An advantage of the present model is that it produces and retains the high ^{230}Th and ^{231}Pa

excesses without any additional assumptions regarding the porosity structure in the shallow part of the system.

6. Concluding remarks

We find that cpx/carbonatite partition coefficients for alkali earth elements, REEs, HFSEs, U, and Th are smaller at the depths of first generation of trace carbonatitic melt in the upwelling mantle as compared to those at shallower depths, but garnet/carbonatite partition coefficients are similar to previous estimates at lower pressures. Owing to higher modal abundance of garnet, the bulk partition coefficients of these elements between peridotite and carbonatitic melt is less extreme. Some consequences of the newly determined partition coefficients include—

1. The proportion of highly incompatible elements that can be removed by extraction of 0.1% carbonatite melt is no more than 30–40%, but key parent/daughter element fractionations can produce reservoirs with distinct Rb/Sr, U/Pb, Th/U, and Sm/Nd ratios. If derived from PM, carbonatite metasomatism can cause an enriched reservoir similar to EM1.
2. The trace element characteristics of the initially formed garnet lherzolite-derived carbonatite melts are unlike erupted carbonatites, most notably in having lower REE and less extreme Nb/Ta. As such melts percolate through the mantle to regions of lower garnet content, melt rock reaction can produce liquids with elevated HREEs as observed in natural carbonatites. However, all the trace element characteristics of carbonatites seem to require involvement of enriched source and/or late stage crystal fractionation and liquid immiscibility.
3. The measured range of CO_2 content in global MORB dataset can simply be explained by mixing of 0.04–13% carbonatitic melt with 45 wt.% CO_2 . However, distribution of CO_2/Nb ratio in MORBs indicates contribution from a melt with much less extreme CO_2/Nb ratio, but high $(\text{La}/\text{Sm})_{\text{N}}$. We postulate that the addition of carbon to MORB or MORB source takes place through addition of carbonated silicate melts, with much lower CO_2/Nb ratio, rather than by addition of carbonatitic melt.
4. Finally, carbonatites beneath mid-oceanic ridges form under conditions where $D_{\text{U}}^{\text{lherzolite/melt}}/D_{\text{Th}}^{\text{lherzolite/melt}}$ and $D_{\text{U}}^{\text{lherzolite/melt}}/D_{\text{Pa}}^{\text{lherzolite/melt}} > 1$, and contributions of 0.03–0.1%, fast-moving carbonatitic melt can potentially account for the observed activity ratios of $(^{230}\text{Th}/^{238}\text{U})$ and $(^{231}\text{Pa}/^{235}\text{U})$ in MORB.

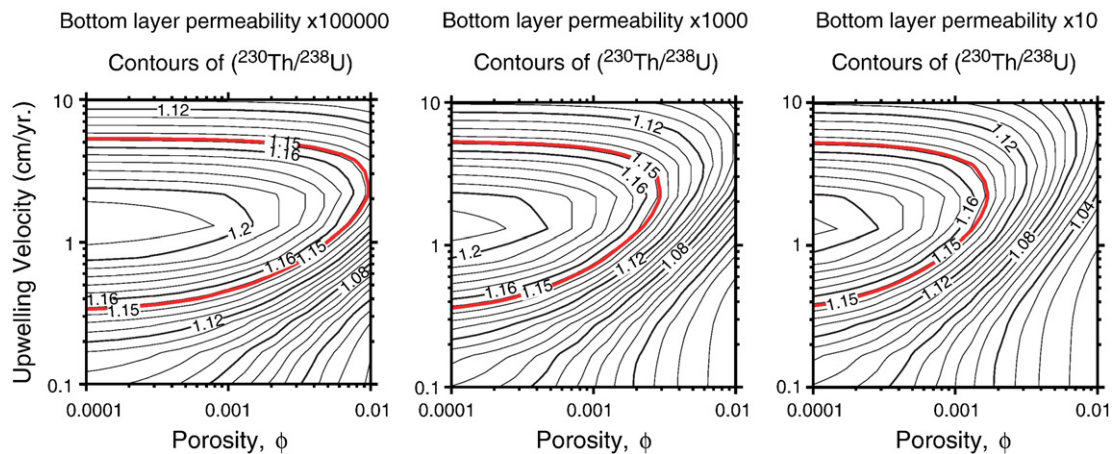


Fig. 16. Contours of ^{230}Th -excesses for melts generated using the garnet lherzolite/carbonatitic melt partition coefficients estimated in this study and the spinel peridotite/basaltic melt partition coefficients from the compilation of Kelemen et al. (2003). The upwelling velocities and a range of initial porosity are varied from 0.1 to 1 cm/year and from 0.01 to 1% respectively. The melting model used is that of Spiegelman and Elliot (1993), using the Web-based program UserCalc (Spiegelman, 2000). Bold lines in red represent 15% ^{230}Th -excess, which is the average excess of MORB. The calculation shows that if the permeability in the deeper part of the melting column is 10 to 10^5 times higher than the basaltic melt dominated top layer, up to 15% ^{230}Th -excess can be created in the erupted melt with porosity varying between 0.1 and 1% and upwelling velocity of 2–3 cm/year. (For interpretation of the references to colour in this figure legend, the reader is referred to the web version of this article.)

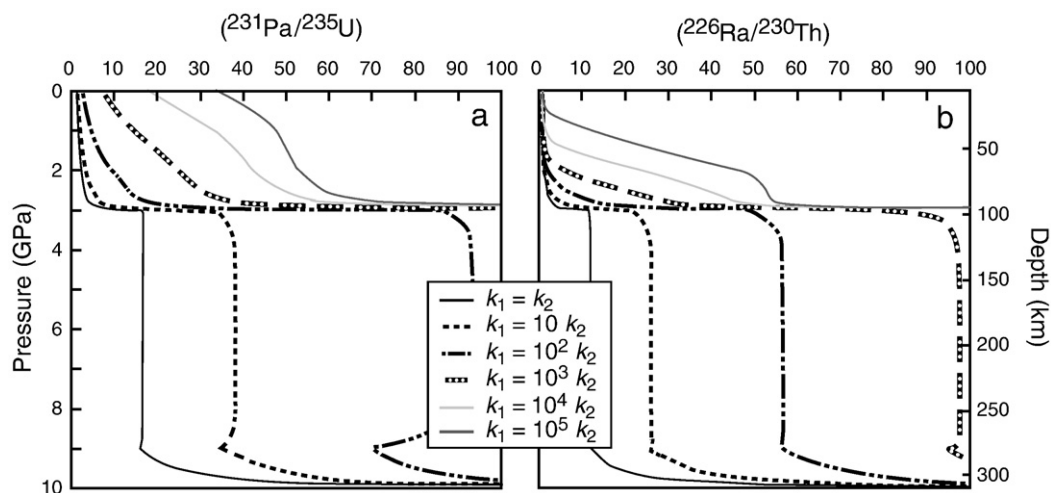


Fig. 17. The depth profiles of (a) the calculated $(^{231}\text{Pa}/^{235}\text{U})$ activity ratio and (b) $(^{226}\text{Ra}/^{230}\text{Th})$ activity ratio, using the model of Spiegelman and Elliot (1993) and the model parameters presented in Fig. 14. Significant ^{231}Pa excesses coming from deep carbonate melt can be preserved in the erupted MORB (a), but owing to short half-life of ^{226}Ra , high $(^{226}\text{Ra}/^{230}\text{Th})$ activity ratio of deep carbonate melt dies down and no more than 15–20% ^{226}Ra excesses can be preserved in the erupted MORB (b).

Acknowledgements

We gratefully acknowledge comments from the editor Jackie Dixon and formal reviews by Fred Frey and an anonymous reviewer. This work received support from Lamont-Doherty Earth Observatory post-doctoral fellowship and Rice University start-up grant to RD, National Science Foundation grants EAR030142 and EAR0609967 to MMH and ACW, 033762 and 0739006 to WFM, and EAR061013 to MS.

References

- Achterbergh, E.V., Ryan, C.G., Jackson, S.E., Griffin, W.L., 2001. Data reduction software for LA-ICP-MS. In: S.P. (Ed.), *Laser Ablation-ICP-MS in the Earth Sciences*. Mineralogical Association of Canada, p. 243.
- Adam, J., Green, D.H., 2001. Experimentally determined partition coefficients for minor and trace elements in peridotite minerals and carbonatitic melt, and their relevance to natural carbonatites. *Eur. J. Mineral.* 13, 815–827.
- Aubaud, C., Hauri, E.H., Hirschmann, M.M., 2004. Hydrogen partition coefficients between nominally anhydrous minerals and basaltic melts. *Geophys. Res. Lett.* 31, L20611. doi:10.1029/2004GL021341.
- Bizimis, M., Salters, V.J.M., Dawson, J.B., 2003. The brevity of carbonatite sources in the mantle: evidence from Hf isotopes. *Contrib. Mineral. Petrol.* 145, 281–300.
- Bizimis, M., Sen, G., Salters, V.J.M., 2004. Hf–Nd isotope decoupling in the oceanic lithosphere: constraints from spinel peridotites from Oahu, Hawaii. *Earth Planet. Sci. Lett.* 217, 43–58.
- Blundy, J.D., Wood, B.J., 1994. Prediction of crystal–melt partition coefficients from elastic moduli. *Nature* 372, 452–454.
- Blundy, J.D., Dalton, J., 2000. Experimental comparison of trace element partitioning between clinopyroxene and melt in carbonate and silicate systems, and implications for mantle metasomatism. *Contrib. Mineral. Petrol.* 139, 356–371.
- Blundy, J.D., Wood, B.J., 2003. Partitioning of trace elements between crystals and melts. *Earth Planet. Sci. Lett.* 210, 383–397.
- Brenan, J.M., Watson, E.B., 1991. Partitioning of trace elements between carbonate melt and clinopyroxene and olivine at mantle P – T conditions. *Geochim. Cosmochim. Acta* 55, 2203–2214.
- Brey, G.P., Kohler, T., Nickel, K.G., 1990. Geothermobarometry in four-phase lherzolites I. experimental results from 10 to 60 kb. *J. Petrol.* 31, 1313–1352.
- Brey, G.P., Bulatov, V.K., Girnis, A.V., 2008. Geobarometry for peridotites: experiments in simple and natural systems from 6 to 10 GPa. *J. Petrol.* 49, 3–24.
- Brice, J.C., 1975. Some thermodynamic aspects of growth of strained crystals. *J. Cryst. Growth* 28, 249–253.
- Cartigny, P., Pineau, F., Aubaud, C., Javoy, M., 2008. Towards a consistent mantle carbon flux estimate: insights from volatile systematics ($\text{H}_2\text{O}/\text{Ce}$, δD , CO_2/Nb) in the North Atlantic mantle (14°N and 34°N). *Earth Planet. Sci. Lett.* 265, 672–685.
- Chakhmouradian, A.R., 2006. High-field-strength elements in carbonatitic rocks: geochemistry, crystal chemistry and significance for constraining the sources of carbonatites. *Chem. Geol.* 235, 138–160.
- Courtney, A.M., Jackson, M.G., Lawrence, J.F., Wang, Z., Lee, C.-T.A., Halama, R., Warren, J.M., Workman, R., Xu, W., Hirschmann, M.M., Larson, A.M., Hart, S.R., Lithgow-Bertelloni, C., Stixrude, L., Chen, W.-P., 2007. Correlation of seismic and petrologic thermometers suggests deep thermal anomalies beneath hotspots. *Earth Planet. Sci. Lett.* 264, 308–316.
- Dalton, J.A., Presnall, D.C., 1998. Carbonatitic melts along the solidus of model lherzolite in the system CaO – MgO – Al_2O_3 – SiO_2 – CO_2 from 3 to 7 GPa. *Contrib. Mineral. Petrol.* 131, 123–135.
- Dasgupta, R., 2006. Experimental investigation of mantle melting in the presence of carbonates. PhD Thesis, University of Minnesota, Minneapolis, 247 pp.
- Dasgupta, R., Hirschmann, M.M., 2006. Melting in the Earth's deep upper mantle caused by carbon dioxide. *Nature* 440, 659–662.
- Dasgupta, R., Hirschmann, M.M., 2007a. Effect of variable carbonate concentration on the solidus of mantle peridotite. *Am. Mineral.* 92, 370–379.
- Dasgupta, R., Hirschmann, M.M., 2007b. A modified iterative sandwich method for determination of near-solidus partial melt compositions. II. Application to determination of near-solidus melt compositions of carbonated peridotite. *Contrib. Mineral. Petrol.* 154, 647–661.
- Dasgupta, R., Hirschmann, M.M., Smith, N.D., 2007. Water follows Carbon: CO_2 incites deep silicate melting and dehydration beneath mid-ocean ridges. *Geology* 35, 135–138. doi:10.1130/G22856A.1.
- Dasgupta, R., Hirschmann, M.M., Withers, A.C., 2004. Deep global cycling of carbon constrained by the solidus of anhydrous, carbonated eclogite under upper mantle conditions. *Earth Planet. Sci. Lett.* 227, 73–85.
- Dobson, D.P., Jones, A.P., Rabe, R., Sekine, T., Kurita, K., Taniguchi, T., Kondo, T., Kato, T., Shimomura, O., Urakawa, S., 1996. In-situ measurement of viscosity and density of carbonate melts at high pressure. *Earth Planet. Sci. Lett.* 143, 207–215.
- Draper, D.S., van Westrenen, W., 2007. Quantifying garnet–melt trace element partitioning using lattice-strain theory: assessment of statistically significant controls and a new predictive model. *Contrib. Mineral. Petrol.* 154, 731–746. doi:10.1007/s00410-007-0235-3.
- Elliot, T., Spiegelman, M., 2003. Melt migration in oceanic crustal production: a U-series perspective. In: Holland, H.D., Turekian, K.K. (Eds.), *Treatise on Geochemistry*. Elsevier Ltd., Amsterdam, pp. 465–510.
- Falloon, T.J., Green, D.H., 1989. The solidus of carbonated, fertile peridotite. *Earth Planet. Sci. Lett.* 94, 364–370.
- Faul, U.H., 2001. Melt retention and segregation beneath mid-ocean ridges. *Nature* 410, 920–923.
- Galer, S.J.G., O'Nions, R.K., 1986. Magmagenesis and the mapping of chemical and isotopic variations in the mantle. *Chem. Geol.* 56, 45–61.
- Green, T.H., Adam, J., Sie, S.H., 1992. Trace element partitioning between silicate minerals and carbonatite at 25 kbar and application to mantle metasomatism. *Mineral. Petrol.* 46, 179–184.
- Gudfinnsson, G., Presnall, D.C., 2005. Continuous gradations among primary carbonatitic, kimberlitic, melilititic, basaltic, picritic, and komatiitic melts in equilibrium with garnet lherzolite at 3–8 GPa. *J. Petrol.* 46, 1645–1659.
- Herzberg, C., Asimow, P.D., Arndt, N., Niu, Y., Leshner, C.M., Fitton, J.G., Cheadle, M.J., Saunders, A.D., 2007. Temperatures in ambient mantle and plumes: constraints from basalts, picrites, and komatiites. *Geochem. Geophys. Geosys.* 8, Q02006. doi:10.1029/2006GC001390.
- Hirschmann, M.M., 2000. The mantle solidus: experimental constraints and the effect of peridotite composition. *Geochem. Geophys. Geosys.* 1 2000GC000070.
- Hirschmann, M.M., Ghiorso, M.S., 1994. Activities of nickel, cobalt, and manganese silicates in magmatic liquids and applications to olivine/liquid and silicate/metal partitioning. *Geochim. Cosmochim. Acta* 58, 4109–4126.
- Hirschmann, M.M., Stolper, E.M., 1996. A possible role of garnet pyroxenite in the origin of the “garnet signature” in the MORB. *Contrib. Mineral. Petrol.* 124, 185–208.
- Hirth, G., Kohlstedt, D.L., 1996. Water in the oceanic upper mantle: implications for rheology, melt extraction and the evolution of the lithosphere. *Earth Planet. Sci. Lett.* 144, 93–108.
- Hoernle, K., Tilton, G., Le Bas, M.J., Duggen, S., Schönberg, D.G., 2002. Geochemistry of oceanic carbonatites compared with continental carbonatites: mantle recycling of oceanic crustal carbonate. *Contrib. Mineral. Petrol.* 142, 520–542.

- Irifune, T., Isshiki, M., 1998. Iron partitioning in a pyrolite mantle and the nature of the 410-km seismic discontinuity. *Nature* 392, 702–705.
- Ito, J., Stixrude, L., 1992. Petrology, elasticity, and composition of the mantle transition zone. *J. Geophys. Res.* 97, 6849–6866.
- Jackson, M.G., Dasgupta, R., 2008. Compositions of HIMU, EM1, and EM2 from global trends between radiogenic isotopes and major elements in ocean island basalts. *Earth Planet. Sci. Lett.* 276, 175–186.
- Jull, M., Kelemen, P.B., Sims, K., 2002. Consequences of diffuse and channelled porous melt migration on uranium series disequilibria. *Geochim. Cosmochim. Acta* 66, 4133–4148.
- Kamber, B.S., Collerson, K.D., 1999. Origin of ocean island basalts: a new model based on lead and helium isotope systematics. *J. Geophys. Res.* 104 (25) 25,479–25,491.
- Kelemen, P.B., Yogodzinski, G.M., Scholl, D.W., 2003. Along strike variation in lavas of the Aleutian island arc: implications for the genesis of high Mg# andesite and the continental crust. In: Eiler, J.M. (Ed.), *Inside the Subduction Factory*. AGU Monograph. American Geophysical Union, Washington, D. C., pp. 223–276.
- Klemme, S., Dalpé, C., 2003. Trace-element partitioning between apatite and carbonatite melt. *Am. Mineral.* 88, 639–644.
- Klemme, S., Meyer, H.-P., 2003. Trace element partitioning between baddeleyite and carbonatite melt at high pressures and temperatures. *Chem. Geol.* 199, 233–242.
- Klemme, S., van der Laan, S.R., Foley, S.F., Gunther, D., 1995. Experimentally determined trace and minor element partitioning between clinopyroxene and carbonatite melt under upper mantle conditions. *Earth Planet. Sci. Lett.* 133, 439–448.
- Kogiso, T., Tatsumi, Y., Nakano, S., 1997. Trace element transport during dehydration processes in the subducted oceanic crust: 1. Experiments and implications for the origin of ocean island basalts. *Earth Planet. Sci. Lett.* 148, 193–205.
- McDonough, W.F., Sun, S.-s., 1995. The composition of the Earth. *Chem. Geol.* 120, 223–253.
- McKenzie, D., Jackson, J., Priestley, K., 2005. Thermal structure of oceanic and continental lithosphere. *Earth Planet. Sci. Lett.* 233, 337–349.
- Nelson, D.R., Chivas, A.R., Chappell, B.W., McCulloch, M.T., 1988. Geochemical and isotopic systematics in carbonatites and implications for the evolution of ocean-island sources. *Geochim. Cosmochim. Acta* 52, 1–17.
- Nowell, G.M., Pearson, D.G., Bell, D.R., Carlson, R.W., Smith, C.B., Kempton, P.D., Noble, S.R., 2004. Hf isotope systematics of kimberlites and their megacrysts: new constraints on their source regions. *J. Petrol.* 45, 1583–1612.
- Perfit, M.R., 1996. Recent volcanism in the Sequeiros transform fault: picritic basalts and implications for MORB magma genesis. *Earth Planet. Sci. Lett.* 141, 91–108.
- Plank, T., Langmuir, C.H., 1992. Effects of melting regime on the composition of the oceanic crust. *J. Geophys. Res.* 97, 19,749–19,770.
- Presnall, D.C., Gudfinnsson, G.H., Walter, M.J., 2002. Generation of mid-ocean ridge basalts at pressures from 1 to 7 GPa. *Geochim. Cosmochim. Acta* 66 (12), 2073–2090.
- Putirka, K.D., 2005. Mantle potential temperatures at Hawaii, Iceland, and the mid-ocean ridge system, as inferred from olivine phenocrysts: evidence for thermally driven mantle plumes. *Geochim. Geophys. Geosys* 6, Q05L08. doi:10.1029/2005GC000915.
- Putirka, K.D., Perfit, M., Ryerson, F.J., Jackson, M.G., 2007. Ambient and excess mantle temperatures, olivine thermometry, and active vs. passive upwelling. *Chem. Geol.* 241, 177–206.
- Pyle, D.M., Dawson, J.B., Ivanovich, M., 1991. Short-lived decay series disequilibria in the natrocarbonatite lavas of Oldoinyo Lengai, Tanzania: constraints on the timing of magma genesis. *Earth Planet. Sci. Lett.* 105, 378–396.
- Saal, A.E., Hauri, E., Langmuir, C.H., Perfit, M.R., 2002. Vapour undersaturation in primitive mid-ocean-ridge basalt and the volatile content of Earth's upper mantle. *Nature* 419, 451–455.
- Salters, V.J.M., Longhi, J., 1999. Trace element partitioning during the initial stages of melting beneath mid-ocean ridges. *Earth Planet. Sci. Lett.* 166, 15–30.
- Salters, V.J.M., Longhi, J.E., Bizimis, M., 2002. Near solidus trace element partitioning at pressures up to 3.4 GPa. *Geochim. Geophys. Geosys.* 3 (7). doi:10.1029/2001GC000148.
- Schmitz, M.D., Vervoort, J.D., Bowring, S.A., Patchett, P.J., 2004. Decoupling of the Lu–Hf and Sm–Nd isotope systems during the evolution of granulitic lower crust beneath southern Africa. *Geology* 32, 405–408.
- Shannon, R.D., 1976. Revised effective ionic radii and systematic studies of interatomic distances in halides and chalcogenides. *Acta Cryst.* A32, 751–767.
- Shaw, H.R., 1972. Viscosities of magmatic silicate liquids: an empirical method of prediction. *Am. J. Sci.* 272, 870–893.
- Spiegelman, M., 2000. UserCalc: a web-based uranium series calculator for magma migration problems. *Geochim. Geophys. Geosys.* 1 1999GC000030.
- Spiegelman, M., Elliot, T., 1993. Consequences of melt transport for uranium series disequilibrium in young lavas. *Earth Planet. Sci. Lett.* 118, 1–20.
- Sweeney, R.J., Green, D.H., Sie, S.H., 1992. Trace and minor element partitioning between garnet and amphibole and carbonatitic melt. *Earth Planet. Sci. Lett.* 113, 1992.
- Sweeney, R.J., Prozesky, V., Przybylowicz, W., 1995. Selected trace and minor element partitioning between peridotite minerals and carbonatite melts at 18–46 kb pressure. *Geochim. Cosmochim. Acta* 59, 3671–3683.
- van Westrenen, W., Draper, D.S., 2007. Quantifying garnet–melt trace element partitioning using lattice-strain theory: new crystal–chemical and thermodynamic constraints. *Contrib. Mineral. Petrol.* 154, 717–730. doi:10.1007/s00410-007-0222-8.
- van Westrenen, W., Blundy, J., Wood, B.J., 1999. Crystal–chemical controls on trace element partitioning between garnet and anhydrous silicate melt. *Am. Mineral.* 84, 838–847.
- van Westrenen, W., Blundy, J.D., Wood, B.J., 2000. Effect of Fe²⁺ on garnet–melt trace element partitioning: experiments in FCMA and quantification of crystal–chemical controls in natural systems. *Lithos* 53, 191–203.
- Walter, M.J., 1998. Melting of garnet peridotite and the origin of komatiite and depleted lithosphere. *J. Petrol.* 39, 29–60.
- Wark, D.A., Williams, C.A., Watson, E.B., Price, J.D., 2003. Reassessment of pore shapes in microstructurally equilibrated rocks, with implications for permeability of the upper mantle. *J. Geophys. Res.* 108, 2050. doi:10.1029/2001JB001575.
- Wood, B.J., Blundy, J.D., 2001. The effect of cation charge on crystal–melt partitioning of trace elements. *Earth Planet. Sci. Lett.* 188, 59–71.
- Workman, R.K., Hart, S.R., 2005. Major and trace element composition of the depleted MORB mantle (DMM). *Earth Planet. Sci. Lett.* 231, 53–72.
- Yaxley, G.M., Green, D.H., 1994. Experimental demonstration of refractory carbonate-bearing eclogite and siliceous melt in the subduction regime. *Earth. Planet. Sci. Lett.* 128, 313–325.